Influence of nitrogen oxides and volatile organic compounds emission changes on tropospheric ozone variability, trends and radiative effect

Suvarna Fadnavis[1], Yasin Elshorbany[2], Jerald Ziemke[3], Brice Barret[4], Alexandru Rap[5], PR Satheesh Chandran [1], Richard J. Pope[6], Vijay Sagar[1], Domenico Taraborrelli[7], Eric Le Flochmoen[4], Juan Cuesta[8], Catherine Wespes[9], Folkert Boersma[10,11], Isolde Glissenaar[10], Isabelle De Smedt[12], Michel Van Roozendael[12], Hervé Petetin[13], Isidora Anglou[10]

[1]Center for Climate Change Research, Indian Institute of Tropical Meteorology, MoES, Pune, India
[2]School of Geosciences, College of Arts and Sciences, University of South Florida, St. Petersburg, FL, USA
[3]NASA Goddard Space Flight Center, Greenbelt, Maryland, USA
[4]LAERO/OMP, Université Paul Sabatier, Université de Toulouse-CNRS, Toulouse, France
[5]School of Earth and Environment, University of Leeds, Leeds, UK;
[6]National Centre for Earth Observation, University of Leeds, Leeds, UK
[7]Institute of Climate and Energy Systems, ICE-3: Troposphere, Forschungszentrum Jülich GmbH, Jülich, Germany,
[8]University Paris Est Creteil and Université Paris Cité, CNRS, LISA, F-94010 Créteil, France
[9]Université libre de Bruxelles (ULB), Spectroscopy, Quantum Chemistry and Atmospheric Remote Sensing, Brussels, Belgium
[10]Royal Netherlands Meteorological Institute (KNMI), De Bilt, The Netherlands
[11]Wageningen University, Environmental Sciences Group, Wageningen, The Netherlands
[12]Belgian Institute for Space Aeronomy, Brussels, Belgium
[13]Barcelona Supercomputing Center, Barcelona, Spain

Corresponding author email: suvarna@tropmet.res.in

Abstract

Ozone in the troposphere is a prominent pollutant whose production is sensitive to the emissions of nitrogen oxides (NOx) and volatile organic compounds (VOC). Here, we assess the variation of tropospheric ozone levels, trends, ozone photochemical regimes, and radiative effects using the ECHAM6–HAMMOZ chemistry-climate model for the period 1998–2019 and satellite measurements. The global mean simulated trend in Tropospheric Column Ozone (TRCO) for the study period (1998–2019) is 0.89 ppb decade^{-1}. During the overlapping period with OMI/MLS observations (2005–2019), the simulated global mean TRCO trends (1.58 ppb decade^{-1}) show fair agreement with OMI/MLS estimates (1.4 ppb decade^{-1}). The simulations for doubling emissions of NOx (DoubNOx), VOCs (DoubVOC), halving of emissions NOx (HalfNOx) and VOCs (HalfVOC) show nonlinear responses to ozone trends and tropospheric ozone photochemical regimes. The DoubNOx simulations show VOC–limited regimes over Indo-Gangetic-Plains, Eastern-China, Western-Europe, and the Eastern-US, while HalfNOx simulations show NOx–limited regimes over North-America and Asia. Emissions changes in NOx (DoubNOx/HalfNOx) influence the shift in tropospheric ozone photochemical regimes compared to VOCs (DoubVOC/HalfVOC).

Further, we provide estimates of tropospheric ozone radiative effects (TO3RE). The estimated global mean TO3RE during 1998–2019 from the CTL simulations is 1.21 Wm^{-2}. The global mean TO3RE shows enhancement by 0.36 W m^{-2} in DoubNOx simulations than CTL. While TO3RE shows a reduction in other simulations compared to CTL (DoubVOC: -0.005 Wm^{-2}; HalfNOx: -0.12 Wm^{-2}; and HalfVOC: -0.03 Wm^{-2}). We show that emissions changes in anthropogenic NOx cause higher changes in TO3RE than anthropogenic VOCs.

Key words: Tropospheric ozone, trends, ozone photochemical regimes; ozone radiative effect. FNR; ECHAM6-HAMMOZ model simulations.

1. Introduction

Tropospheric ozone, a major air pollutant, has been a pressing issue in recent decades due to its detrimental effect on human health and ecosystem productivity and as a short-term climate forcer (Riese et al. 2012; Gulev et al., 2021; Wang et al., 2022). Considering these harmful impacts, the assessment of tropospheric ozone levels and trends are being conducted frequently (Gaudel et al., 2018; Mills et al., 2018; Tarasick et al., 2019). Ozone trends are being assessed from surface observations, in-situ and ground-based measurements, satellite retrievals, and model simulations (Cooper et al., 2014; Cohen et al., 2018; Young et al., 2018; Tarasick et al., 2019; Archibald et al., 2020). The latest IPCC AR6 reported an enhancement in free tropospheric ozone by $2-7\%$ decade^{-1} in the northern mid-latitudes, $2-12\%$ per decade in the tropics, and $<5\%$ decade^{-1} in southern mid-latitudes (Gulev et al., 2021; Szopa et al., 2021). The Tropospheric Ozone Assessment Reports (TOAR) have documented global increases of tropospheric column ozone (TRCO) in the 20th century (Cooper et al., 2014; Lefohn et al., 2017; Schultz et al., 2017; Fleming et al., 2018; Gaudel et al., 2018; Mills et al., 2018; Young et al., 2018; Tarasick et al., 2019). Increasing tropospheric trends are explained by enhanced anthropogenic emissions (Cooper et al., 2014; Zhang et al., 2016) and modulation by climate variability (Lin et al., 2014; Lu et al., 2018). Several studies have documented increasing trends in TRCO across various regions and different time periods.

For instance, enhancement in TRCO trends globally using measurements from multiple sources such as In-service Aircraft for a Global Observing System database (IAGOS) and ozonesondes and GEOS–Chem model simulation revealed an increasing trend of 2.7 ± 1.7 and 1.9 ± 1.7 ppb decade^{-1} between 1995 and 2017 (Wang et al., 2022). Additionally, Fiore et al. (2022) also found increasing trends ranging from 0.6 to 2.5 ppb decade^{-1} from 1950 to 2014 globally based on the available limited surface ozone records and the Community Earth System, version-2, the Whole Atmosphere Community Climate Model, version-6 (CESM2–WACCM6) model study. Furthermore, trends in TRCO are stronger in the Northern Hemisphere (NH) than Southern Hemisphere (SH) due to larger anthropogenic emissions (Monks et al., 2015). Ozone Monitoring Instrument (OMI) and Microwave Limb Sounder (MLS) observations from 2005 until 2010 show annual TRCO burden averaged over the NH exceeds the SH by 4% at low latitudes ($0°-25°$), by 12% at mid-latitudes ($25°-50°$), and by 18% at high latitudes ($50°-60°$) (Cooper et al., 2014). CMIP6 models also show that the

93   tropospheric ozone burden increased by 44 % in 2005 – 2014 compared to 1850 (Griffiths et
94   al., 2021). Recently, studies have reported a decrease in TRCO trends globally after the
95   Corona–Virus Disease 2019 (COVID–19) outbreak e.g., Chang et al. (2022, 2023), and
96   Steinbrecht et al. (2021). Also, Putero et al. (2023) show widespread ozone decreases at high-
97   elevation sites due to the COVID–19 lockdown. However, our study period (1998–2019)
98   excludes the COVID–19 associated emission changes.

99

100   Nitrogen oxides (NOx; $NO+NO_2$) and volatile organic compounds (VOC) are the major
101   precursors that define ozone photochemical regimes (Duncan et al 2010). Information on ozone
102   photochemical regimes is of utmost importance to know ozone (O_3) levels. However, the non-
103   linearity in the O_3 – NOx – VOC chemistry has always posed a challenge in identifying
104   photochemical regimes. The regime is called NOx–limited if the ozone production is directly
105   related to a change in NOx rather than from VOC perturbations. Whereas the region where
106   ozone production is regulated by the ambient availability of VOCs is called VOC–limited
107   (Sillman et al., 1990; Kleinman, 1994). The ratios such as ozone to oxidized nitrogen species
108   (O_3/(NOy-NOx), where NOy is the total reactive nitrogen), formaldehyde to total reactive
109   nitrogen (HCHO/NOy), formaldehyde to nitrogen dioxide ($HCHO/NO_2$), hydrogen peroxide
110   to nitric acid (H_2O_2/HNO_3) are adopted to diagnose the ozone photochemical regimes (e.g.,
111   Sillman, 1995; Martin et al., 2004; Duncan et al., 2010). Among these, the most widely used
112   indicator to identify regimes is the Formaldehyde (HCHO) to Nitrogen dioxide (NO_2) Ratio
113   (FNR) (Martin et al., 2004; Duncan et al., 2010). In our study, we adopt FNR to identify NOx–
114   limited or VOC–limited regimes. On par with the current effort to mitigate ozone pollution, it
115   is important to understand how the changes in emissions of NOx and VOC affect the ozone
116   photochemical regimes and trends (Jin et al., 2017, 2020).

117

118   Ozone is the third strongest anthropogenic greenhouse gas, also called a short-term
119   climate forcer, producing a global average radiative forcing of 0.47 [0.24 to 0.71 W m^{-2}] [5%
120   to 95% uncertainty range] (Forster et al., 2021). Recent studies showed ozone effective
121   radiative forcing (ERF) of 0.51 [0.25 to 0.76] W m^{-2} during 1750 – 2023 (Forster et al., 2024).
122   The knowledge of ozone radiative forcing due to changes in anthropogenic emissions of NOx
123   and VOC will help to assess climate change. Therefore, we also show the impacts of enhanced
124   or reduced emissions of NOx and VOC on ozone radiative effect in addition to ozone trends

125 and photochemical regimes. To achieve this, we conducted sensitivity experiments by doubling
126 and halving global NOx and VOC emissions using the state–of–the–art chemistry-climate
127 model ECHAM6–HAMMOZ for the period 1998–2019. This approach of increase/decrease of
128 emissions is important to understand the nonlinear response of ozone to emission changes.
129 These experiments are helpful for designing emission implementation strategies (e.g., Zhang
130 et al., 2021; Wang et al., 2023). The paper is outlined as follows: satellite data and the model
131 experimental setup are given in section 2, and results are given in section 3, which includes a
132 comparison of simulated tropospheric column ozone with satellite data and estimated ozone
133 trends. Discussions on ozone photochemical regimes and their trends are made in sections 4 to
134 6. Estimates of ozone radiative effects are given in section 7. Conclusions are made in section
135 8.

136 **2.   Satellite data and model experiments**

137 **2.1.   OMI Satellite Data**.

138 We include OMI/MLS tropospheric column ozone (TRCO) for October 2004 – December 2019
139 and OMI NO_2, HCHO data for latitude range 60° S – 60° N (Ziemke et al., 2006; De Smedt et
140 al., 2021; Lamsal et al., 2021). OMI/MLS TRCO is determined by subtracting MLS
141 stratospheric column ozone (SCO) from OMI total column ozone each day at each grid point.
142 Tropopause pressure used to determine the SCO invoked the World Meteorological
143 Organization (WMO) 2 K km^{-1} lapse-rate definition from the NCEP reanalysis. The MLS data
144 used to obtain SCO were derived from the MLS v4.2 ozone profiles. We estimate 1σ precision
145 for the OMI/MLS monthly mean gridded TRCO product to be about 1.3 DU. Adjustments for
146 drift calibration and other issues (e.g., OMI row anomaly) affecting OMI/MLS TRCO are
147 discussed by Ziemke et al. (2019) and Gaudel et al. (2024).
148 We used OMI monthly mean Level 3 (L3) data for NO_2 and HCHO
149 (https://doi.org/10.18758/h2v1uo6x) that were produced in the context of the ESA CCI+
150 precursors for aerosols and ozone project (De Smedt et al., 2021; Anglou et al., 2024). The
151 datasets consist of the monthly mean tropospheric column densities for NO_2 and HCHO (based
152 on the QA4ECV NO_2 and HCHO dataset) as measured by OMI from October 2004 to March
153 2019, and include minimum spatial and temporal coverage thresholds (De Smedt et al., 2018).
154 OMI has an overpass time of 13.30 local time and the retrieved column densities concern clear-
155 sky or partially cloudy conditions.

156

2.2   IASI–SOFRID

The Software for a Fast Retrieval of Infrared Atmospheric Sounding Interferometer (IASI) data (SOFRID) retrieves global ozone profiles from IASI radiances (Barret et al., 2011, 2021). It is based on the RTTOV (Radiative Transfer for TOVS) operational radiative transfer model jointly developed by ECMWF, Meteo–France, UKMO and KNMI within the NWPSAF (Saunders et al., 1999; Matricardi et al., 2004). The RTTOV regression coefficients are based on line–by–line computations performed using the HITRAN2004 spectroscopic database (Rothman et al., 2005), and the land surface emissivity is computed with the RTTOV UW–IRemis module (Borbas and Ruston, 2010). The IASI–SOFRID ozone for the study period (2008 to 2019) is obtained from METOP–A (2008-2018) and METOP–B (2019).

We use the SOFRID version 3.5 data presented and validated in Barret et al. (2021), which uses dynamical a priori profiles from an O_3 profile tropopause-based climatology according to tropopause height, month, and latitude (Sofieva et al., 2014). The use of such an a priori has largely improved the retrievals, especially in the SH where the previous version was biased. The retrievals are performed for clear-sky conditions (cloud cover fraction < 20%). IASI–SOFRID ozone retrievals provide independent pieces of information in the troposphere, the UTLS (300 – 150 hPa), and the stratosphere (150 – 25 hPa) (Barret et al., 2021). SOFRID TRCO absolute biases relative to ozonesondes are lower than 8 % with root mean square error (RMSE) values lower than 18 % across the six 30° latitude bands (see Barret et al. (2021)). Importantly, Barret et al. (2021) have shown that relative to ozonesondes, TRCO from IASI–SOFRID display no drifts (<2.1 % decade^{-1}) for latitudes lower than 60°N and in the SH for latitudes larger than 30° (<3.7 % decade^{-1}). But significant drifts are observed in the SH tropics (-5.2% decade^{-1}) and in the NH at high latitudes (12.8% decade^{-1}).

2.3   IASI+GOME2

IASI+GOME2 is a multispectral approach to retrieve the vertical profile of ozone and its abundance in several partial columns. It is based on the synergy of IASI and GOME2 spectral measurements in the thermal infrared and ultraviolet spectral regions, respectively, which are jointly used to improve the sensitivity of the retrieval for the lowest tropospheric ozone (below

3 km above sea level, see Cuesta et al., 2013). Studies over Europe and East Asia have shown particularly good capabilities for capturing near-surface ozone variability compared to surface in situ ozone measurements (Cuesta et al., 2018, 2022; Okamoto et al., 2023). TRCOs from IASI–GOME2 also show good agreement with several datasets of in-situ measurements for a four-year period in the tropics, with almost negligible biases and high correlations (Gaudel et al., 2024). This ozone product provides global coverage for low cloud fraction conditions (below 30%) for 12 km diameter pixels spaced 25 km apart (at nadir). The IASI–GOME2 global dataset is publicly available through the French AERIS data center, with data from 2017 to the present and covers the 90° S – 90° N latitude band. For this study, we use the monthly TRCO data between the surface and the tropopause for 2017 – 2019 for different latitude bands.

2.4   TROPOMI

The TROPOspheric Monitoring Instrument (TROPOMI) is the sole payload on the Copernicus Sentinel–5 Precursor (Sentinel–5P or S5P) satellite, which provides measurements of multiple atmospheric trace species, including NO_2 and HCHO, at high spatial and temporal resolutions (Veefkind et al., 2012). TROPOMI has a daily global coverage with a spatial resolution of 5.5 $\times$ 3.5 km^2 at nadir since a long-track pixel size reduction on 6 August 2019. We have used the ESA CCI+ Level–3 gridded 1° x 1° monthly tropospheric column of NO_2 (based on L2 v2.3.1, which applies a retrieval consistent with the most recent TROPOMI L2 version) and HCHO (https://doi.org/10.18758/2imqez32) (based on L2 v2.4.1, collection 3) data from May 2018 to December 2019 for our study (De Smedt et al., 2021; Glissenaar et al., 2024). This dataset was created using the same methods as the ESA CCI+ OMI Level–3 datasets.

2.5   The ECHAM6-HAMMOZ model experiments

The ECHAM6.3–HAM2.3–MOZ1.0 aerosol chemistry–climate model (Schultz et al., 2018) used in the present study comprises the general circulation model ECHAM6 (Stevens et al., 2013), the tropospheric chemistry module, MOZ (Stevenson et al., 2006) and the aerosol module, Hamburg Aerosol Model (HAM) (Vignati et al., 2004). The gas phase chemistry is represented by the Jülich Atmospheric Mechanism (JAM) v002b mechanism (Schultz et al., 2018). This scheme is an update and an extension of terpenes and aromatics oxidation based on the MOZART–4 model (Emmons et al., 2010) chemical scheme. Tropospheric heterogeneous chemistry relevant to ozone is also included (Stadtler et al., 2018). MOZ uses

the same chemical preprocessor as CAM–Chem (Lamarque et al., 2012) and WACCM (Kinnison et al., 2007) to generate a FORTRAN code containing the chemical solver for a specific chemical mechanism. Land surface processes are modelled with JSBACH (Reick et al., 2013). Biogenic VOC emissions are modelled with the MEGAN algorithm (Guenther et al., 2012) which has been coupled to JSBACH (Henrot et al., 2017). The lightning NOx emissions are parameterized in the ECHAM6–HAMMOZ as described by Rast et al. (2014). The lightning parameterization is the same in all the simulations. The model simulations were performed for the period 1998 to 2019 using the Atmospheric Chemistry and Climate Model Intercomparison Project (ACCMIP) (Lamarque et al., 2010; Van Vuuren et al., 2011) emission inventory. ACCMIP emission inventory includes emissions from agriculture and waste burning, forest and grassland fires, aircraft, domestic fuel use, energy generation including fossil fuel extraction, industry, ship traffic, solvent use, transportation, and waste management. The model was run at a T63 spectral resolution corresponding to about $1.8° \times 1.8°$ in the horizontal dimension and 47 vertical hybrid $\sigma – p$ levels from the surface up to 0.001 hPa. The details of model parameterizations and validation are described by (Fadnavis et al., 2019b, 2019a, 2021b, 2021a, 2022, 2023). We performed five experiments: (1) control (CTL) and four emission sensitivity experiments: (2) doubling anthropogenic emission of NOx globally (DoubNOx), (3) reducing anthropogenic emissions of NOx by 50 % globally (HalfNOx), (4) doubling anthropogenic emissions of all VOCs globally (DoubVOC), (5) reducing anthropogenic emissions of all VOCs by 50 % globally (HalfVOC). We performed each experiment from 1998 to 2019 after a spin-up of one year. We used the Representative Concentration Pathway (RCP) 8.5 high emission scenario (Van Vuuren et al., 2011) in all model simulations. In each experiment, the monthly varying AMIP–II sea surface temperature and sea ice representative of the period 1998–2019 were specified as a lower boundary condition. Anthropogenic VOC emissions included in the model are listed in the supplementary table S1.

TRCO is computed from the satellite data and model simulations by averaging O_3 amounts from the surface up to the tropopause. The partial tropospheric column is converted into a mixing ratio assuming a constant ozone mixing ratio in the troposphere. Tropopause considered is as described by the WMO thermal tropopause definition, the lowest level at which the temperature lapse rate decreases to 2 K km^{-1} or less (WMO, 1957). The estimated tropopause in the satellite data will show differences since the tropopause is quite variable in space and

249   time; its location will depend on the employed reanalysis (e.g., Hoffmann and Spang, 2022).

250   The vertical resolution of the satellite and the ECHAM6-HAMMOZ also affect the estimated

251   tropopause. For comparison of the model with satellite datasets, e.g., IASI–SOFRID,

252   OMI/MLS, we use model and satellite data for the same period.

253

254   **2.6   Tropospheric ozone radiative effects**

255   The tropospheric ozone radiative effect (TO3RE) is calculated as in Pope et al. (2024). While

256   the radiative effect calculated in ECHAM6–HAMMOZ also includes impacts of aerosols and

257   dynamical effects, here we isolate TO3RE by using the Rap et al. (2015) tropospheric ozone

258   radiative kernel derived from the SOCRATES offline radiative transfer model (Edwards and

259   Slingo, 1996), including stratospheric temperature adjustments. To calculate the TO3RE, the

260   monthly averaged ECHAM6–HAMMOZ simulated ozone field is multiplied by the offline

261   radiative kernel (at every grid box). It is then summed from surface to the tropopause. The

262   simulated ozone data are mapped onto the spatial resolution of the radiative kernel and then

263   interpolated vertically onto its pressure grid. The equation for each grid box is

264     $TO3RE = \sum_{i=surf}^{trop} RK_i \times O_{3i} \times dp_i /100$ (1)

265   where TO3RE is the tropospheric ozone radiative effect (W m^{-2}), RK is the radiative kernel

266   (W m^{-2} ppbv^{-1} 100 hPa^{-1}), O_3 is the simulated ozone grid box value (ppbv), dp is the pressure

267   difference between vertical levels (hPa), and 'i' is the grid box index between the surface

268   pressure level and the tropopause pressure. The tropopause pressure is identified based on the

269   WMO lapse rate tropopause definition. Several past studies have used this approach of using

270   the SOCRATES offline radiative kernel with output from model simulations to derive the

271   TO3RE (Rap et al., 2015; Scott et al., 2018; Rowlinson et al., 2020; Pope et al., 2024).

272   **3. Results**

273   **3.1 Comparison of the simulated seasonal cycle in TRCO, NO₂ and HCHO with**
274   **satellites retrievals**

275   In this section, we compare the estimated TRCO from the model (CTL) simulation with

276   OMI/MLS (2005 – 2019), IASI–SOFRID (2008 – 2019), and IASI–GOME2 (2017 – 2019)

277   satellite retrievals. We compared simulated TRCO for the same period as individual satellite

278   retrievals. The comparison of monthly mean TRCO is made for 20° latitude bins in Figure 1.

In the northern tropics (0° N – 20° N) (Fig. 1a), the OMI/MLS data exhibits an annual cycle with a peak in April, whereas the model indicates a peak in January. Both datasets show a minimum in August. The model underestimates TRCO by 1.8 to 3.9 ppb during March to October. In the 21° N – 40° N and 41° N – 60° N latitude bands (Fig. 1 b–c), the model shows a one-month lead in the peak of the annual cycle compared to OMI/MLS. In the 21° N – 40° N band, the model underestimates OMI/MLS TRCO by 2.8 – 6.1 ppb during the summer months (May–August), while it overestimates TRCO by 4.1 – 8.3 ppb from October to March. The 41° N – 60° N latitude band exhibits an underestimation in the model by 1.1 – 6.3 ppb during June and July, while it overestimates (0.7 – 7.5 ppb) the rest of the year. In the Southern Hemisphere (SH), OMI/MLS and the model show a similar pattern in the seasonal cycle. The model shows a one-to-two-month lead in the annual cycle. However, the model shows an underestimation of TRCO for all months. The model underestimates TRCO by 0.5 to 7.1 ppb in the 0 – 20 °S, by 5.1– 15.3 ppb in 21° S – 40° S, and by 9.2 – 13.8 ppb in the 41° S – 60° S latitude bands. The comparison of TRCO from IASI–SOFRID with the model shows features similar to those in the OMI/MLS. In the 0° N – 20° N latitude band, the model underestimates the TRCO by about 3.8 to 7.7 ppb from April to October and in the 21° N – 60° N latitude band by 1.9 – 11.3 ppb in summer (May–August). In the SH, the model shows better agreement with IASI–SOFRID than OMI/MLS. During the SH winter (June–August), the model overestimates TRCO by 2.8 – 6.5 ppb in the latitude range of 0° S – 40° S. Conversely, it underestimates TRCO by 2.7 – 8.2 ppb in the 41° S – 60° S throughout the year, which is less compared to other satellite datasets. IASI–SOFRID is known to suffer from negative drifts in the SH (Barret et al., 2021).

Interestingly, the model exhibits a fair agreement with IASI–GOME2 retrieved TRCO during the summer months (May–August) in the Northern Hemisphere (NH). During the winter months, the estimated TRCO shows a large overestimation of 8.3 – 11.7 ppb in the NH (0° N – 40° N), while it is underestimated by 8.3 – 11.7 ppb in the 41° N – 60° N. In the SH, a fairly good agreement is observed between the model and IASI–GOME2 TRCO, especially in the 0° S – 40° S latitude band. The model overestimates the TRCO by 7.4 – 8.8 ppb in the 0° S – 20° S during SH winter and underestimates by 4.7 – 6.7 ppb in the 21° S – 40° S belt during SH summer (December–January–February). An overall underestimation of about 7 – 11.2 ppb in TRCO is noted in the 41° S – 60° S throughout the year. Figure 1 shows that a peak in the seasonal cycle in the model is earlier than the three satellite data between 40° N and 40° S. In

311 general, the model underestimates TRCO in summer in the NH and overestimates in winter
312 relative to OMI/MLS, and IASI–SOFRID. In the SH, the model underestimates TRCO
313 throughout the year compared to OMI/MLS, IASI–SOFRID, and IASI–GOME2, especially in
314 the 41° N – 60° N band. Although the model–satellite comparison is done for the same period,
315 the differences in sampling between the model and satellite measurements may cause the
316 observed differences. It should be noted that the spatial resolution, coverage, and diurnal
317 sampling time differ among the satellites which also contribute to the observed differences
318 among them.

319
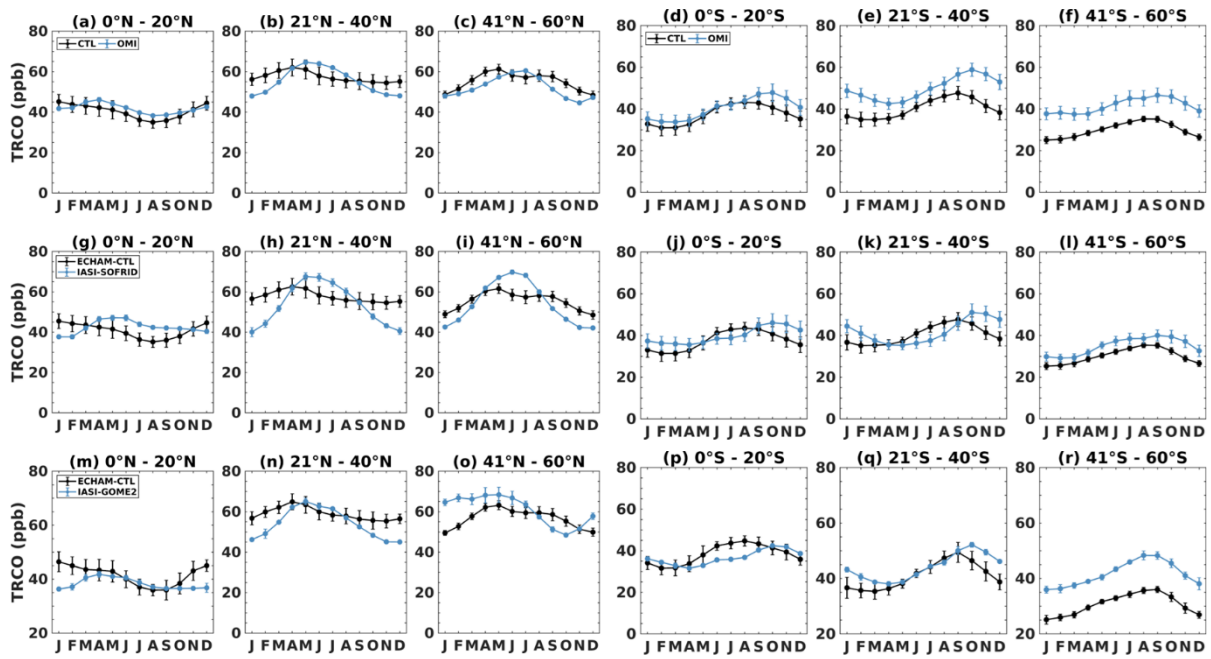
330 Figure 1. Time series of monthly mean TRCO (ppb) averaged for 20° wide latitude bins from
331 (a–f) OMI/MLS (blue) and ECHAM6–HAMMOZ CTL simulations (black) for the time period
332 October 2004 – December 2019. (g–l) same as (a–f) but for IASI–SOFRID (blue) and
333 ECHAM6–HAMMOZ CTL simulations (black) for the period January 2008 – December 2019,
334 and (m–r) same as (a–f) but for IASI–GOME2 (blue) and ECHAM6–HAMMOZ CTL
335 simulations (black) for the time period January 2017 – December 2019. The vertical bars in all
336 the figures represent 2σ standard deviation.

337

338 To evaluate our model simulations of NO$_2$ and HCHO, we compare the simulated tropospheric
339 column NO$_2$ and HCHO with the ESA CCI+ monthly averaged TROPOMI and OMI data (Fig.
340 2). The simulated NO$_2$ reproduces the seasonal cycle but shows overestimation in the entire
341 latitude band except 41° S – 60° S in the SH. In the NH, the magnitude of overestimation in
342 the simulated NO$_2$ increases with latitude. Simulated NO$_2$ is overestimated by 0.15 to 0.35

343    $\times 10^{15}$ molecules cm^{-2} in 0° N – 20° N, by 0.3 to 0.6 $\times 10^{15}$ molecules cm^{-2} in 21° N – 40° N,

344   and by 0.25 to 0.9 $\times 10^{15}$ molecules cm^{-2} in 41° N – 60° N latitude bands compared to

345   TROPOMI. Similarly, simulated NO$_2$ is overestimated compared to OMI by 0.16 to 0.35 $\times 10^{15}$

346   molecules cm^{-2} in 0° N – 20° N, by 0.16 to 0.48 $\times 10^{15}$ molecules cm^{-2} in 21° N – 40° N, and

347   by 0.18 to 0.76 $\times 10^{15}$ molecules cm^{-2} in 41° N – 60° N latitude belt (Fig. 2a–c and 2g–i).

348   Although the model overestimates NO$_2$ in the SH, the magnitude of this overestimation is

349   smaller compared to NH. Simulated NO$_2$ shows a fairly good agreement from 21° S to 60° S

350   latitudes in the SH (Fig. 2d–f and 2j–l).
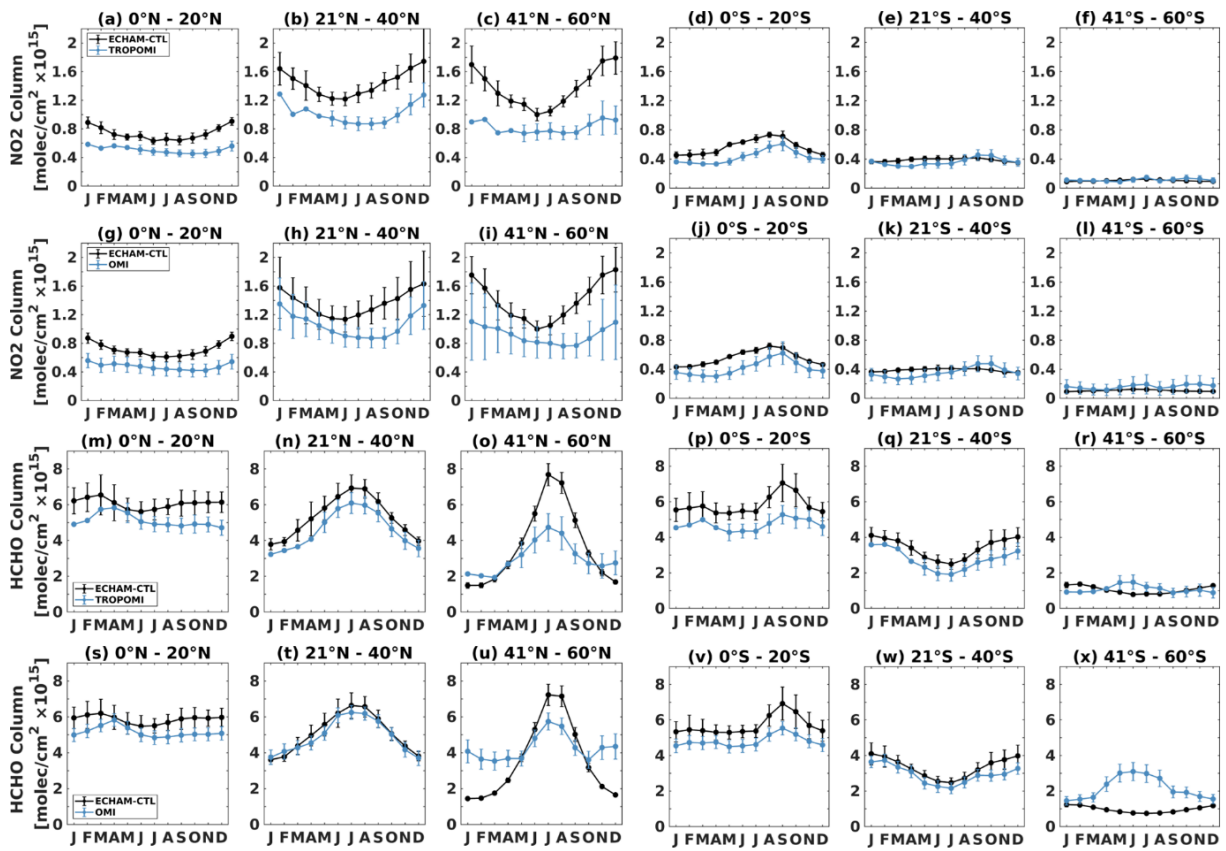
Figure 2. Time series of monthly mean tropospheric column NO$_2$ (molecules/cm^2) averaged
for 20° wide latitude bins from ECHAM6–HAMMOZ CTL simulations (black) for the time
period same as (a–f) TROPOMI from May 2018 to December 2019, and (g–l) OMI from
January 2005 to December 2019. (m–x) are the same as that of (a–l) but for HCHO. The vertical
bars in the figures represent 2σ standard deviation.

371 While the simulated HCHO successfully reproduces the seasonal cycle in both hemispheres, it

372 shows a large overestimation, particularly in the tropical region (Fig. 2m–x). The

373 overestimation is most pronounced when compared to TROPOMI, especially in the tropics,

374 and to a lesser extent with OMI. The model HCHO aligns reasonably well with both TROPOMI

375 and OMI in the northern and southern mid-latitudes ($21°$ N $– 40°$ N and $21°$ S $– 40°$ S) with a

376 modest overestimation of $0.4 – 1.2 \times 10^{15}$ molecules cm^{-2} and $0.3 – 0.5 \times 10^{15}$ molecules cm^{-2}

377 respectively in the NH and $0.4 – 1 \times 10^{15}$ molecules cm^{-2} and $0.5 – 1.4 \times 10^{15}$ molecules cm^{-2}

378 respectively in the SH. However, in the $41°$ N $– 60°$ N band, the model overestimates HCHO

379 compared to TROPOMI (OMI) by $0.6 – 2.9$ $(0.5–1.7) \times 10^{15}$ molecules cm^{-2} during the NH

380 from May to October and underestimates it by $0.08 – 1.1$ $(0.01 – 2.7) \times 10^{15}$ molecules cm^{-2}

381 during other months. On the contrary, the model underestimates HCHO in the $41°$ S $– 60°$ S

382 during SH winter. It should be noted that TROPOMI/OMI monthly means are valid for clear-

383 sky situations, whereas the model simulations are all-day all-sky averages. In previous studies

384 (Boersma et al. (2016) and references therein), it was shown that NO_2 is typically $15 – 20$ %

385 lower on clear-sky days than under cloudy situations due to higher photolysis rates, and faster

386 chemical loss of NO_2.. Further, OMI and TROPOMI cannot sample for snowy scenes, and

387 nighttime. There is significantly lower coverage on the NH during winter and vice versa for

388 SH. These all can likely cause model and satellite differences. For HCHO the effect is smaller

389 because HCHO is both produced and destroyed by OH (see Fig. 4 in Boersma et al. 2016). In

390 addition, diurnal NO_2 observations from Geostationary Environment Monitoring Spectrometer

391 (GEMS), Edwards et al. (2024) showed that the tropospheric column diurnal NO2 variations

392 can be larger than 50 % of the column amount compared to once-a-day TROPOMI

393 observations. Considering these differences, we proceed with the analysis of TRCO trends,

394 ozone photochemical regimes, and ozone radiative effects.

395

3.2. Impacts of emission changes on the spatial distribution of ozone

397 Figure 3 shows the spatial distribution of the simulated surface (Fig. 3a–e) and TRCO (Fig. 3f–

398 j) concentration from ECHAM CTL simulations and the anomalies obtained from differences

399 in DoubNOx - CTL, DoubVOC - CTL, HalfNOx - CTL, and HalfVOC - CTL simulations for

400 the period 1998 – 2019. The CTL simulation shows high surface ozone levels (19 – 61.1 ppb)

401 between $10°$ N $– 40°$ N (Fig. 3a). Doubling of NOx emission (DoubNOx) causes a global mean

402   enhancement of surface ozone anomalies by 4.1 [-3.8 to 13], [5th to 95th percentile] ppb. Surface

403   ozone anomalies show an increase of 5 – 20 ppb across most of the globe, excluding highly

404   urbanized regions like the Indo-Gangetic plains (IGP), Southeast China, Northeastern United

405   States (US), and Europe. (Fig. 3b). Over these regions, a large reduction (8 – 20 ppb) in surface

406   ozone anomalies is noticed, indicating ozone titration by NOx. While surface ozone anomalies

407   from DoubVOC - CTL simulations show global mean enhancement by 0.9 [0.1 to 2.3] ppb, its

408   magnitude is less than that of the anomalies from DoubNOx - CTL (Fig. 3c). The largest

409   increase in surface ozone anomalies for DoubVOC is observed over IGP, Eastern China and

410   the Eastern US (3 – 6 ppb). Interestingly, these are the same regions where a decrease in ozone

411   anomalies is observed in the DoubNOx case. The decrease (increase) in ozone anomalies with

412   an increase in NOx (VOC) emissions indicates that these regions could be NOx–saturated or

413   VOC–limited. Reduction of NOx emissions (HalfNOx-CTL) simulations show a reduction in

414   surface ozone anomalies (global mean by -2.5 [-7.2 to -0.7] ppb) except over North-Eastern

415   China (Fig. 3d). Earlier, Souri et al. (2017) also reported that eastern Asia has witnessed a rise

416   in surface ozone levels despite NOx control strategies, indicating the prevalence of VOC–

417   limited photochemistry over this region (details in section 4 to 6). However, the absence of

418   such an increase over other VOC–limited regions point towards nonlinear ozone chemistry.

419   While HalfVOC - CTL stimulation causes a reduction in surface ozone anomalies (global mean

420   -0.4 [-1.4 to 0.05] ppb), an increase is observed in South America, some parts of the US,

421   Australia, and the Indo-China peninsula (Fig. 3e). This increase could be due to a reduction in

422   the radical destruction of ozone caused by aromatic hydrocarbons in low NOx conditions in

423   these regions (Taraborrelli et al., 2021).

424

425   Further, we show the impact of emission changes on the TRCO distribution (Fig. 3f–j). The

426   estimated global mean TRCO from the CTL simulation from 1998 to 2019 is 39.4 [23.8 to

427   56.8] ppb (Fig. 3f). CTL simulations show higher amounts of TRCO (40.9 to 68.8 ppb) in the

428   latitudinal band of 20° N to 40° N. These concentrations are pronounced over South and East

429   Asia, spanning from the Mediterranean region to eastern China (Fig. 3f). TRCO anomalies

430   from DoubNOx - CTL show enhancement by 11.7 [6.9 to 19.8] ppb (global mean) (Fig. 3g).

431   Between 20° N – 40° N belt, the TRCO anomalies exceed by 6.1 – 29.3 ppb, particularly over

432   South Asia. Interestingly, in highly urbanized areas such as the IGP, Southeast China,

433   Northeast US, and Europe, there is only a marginal increase in TRCO anomalies (~5 ppb). This

434   suggests the existence of a distinct ozone photochemical regime in these regions. Further

435   exploration of this aspect will be discussed in sections 4 to 6.

436
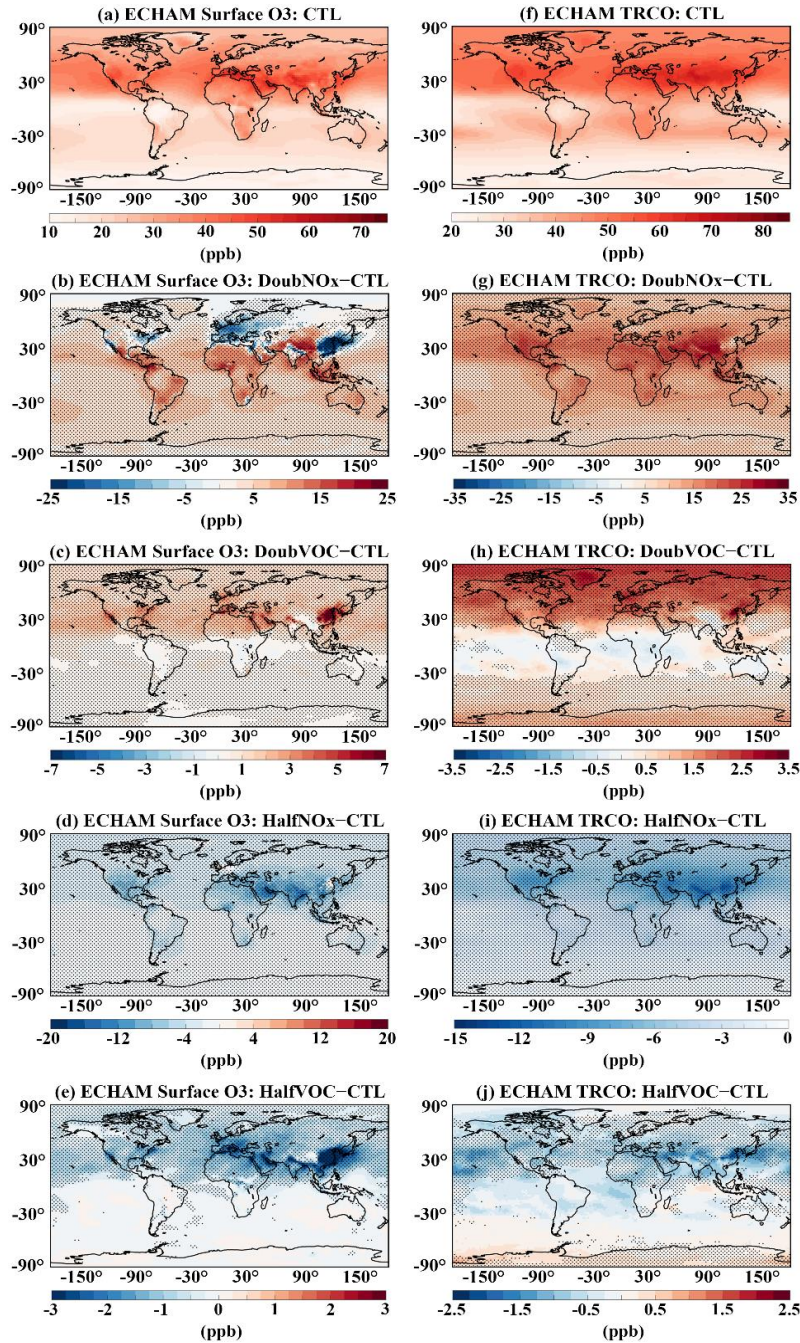
457   Figure 3. Spatial distribution of surface ozone (ppb) for (a) from CTL simulations, anomalies
458   from (b) DoubNOx - CTL, (c) DoubVOC - CTL, (d) HalfNOx - CTL, and (e) HalfVOC - CTL
459   simulations. (f–j) are the same as that of (a–e) but for TRCO. The stippled regions in the figures
460   indicate anomalies significant at 95% confidence based on the t-test.

461   The impact of the doubling of VOC emissions (anomalies from DoubVOC - CTL simulations)
462   on TRCO is depicted in Figure 3h. An increase in global mean TRCO by 1 [-0.2 to 2.4] ppb is
463   observed in this emission scenario. It should be noted that TRCO anomalies from DoubVOC -
464   CTL are ten times less than that from DoubNOx - CTL (Fig. 3g and 3h). Large values of TRCO
465   anomalies (1.5 – 2) are observed in the high latitudes (north of 60° N) and South and East Asia,
466   with the largest values of more than 2.5 ppb over East China (e.g., Beijing). Interestingly, slight
467   decreases in TRCO are seen in the tropical regions. This is consistent with the recent finding
468   that aromatics, especially benzene, can lead to efficient ozone destruction in tropical UTLS
469   (Rosanka et al., 2021). The TRCO anomalies in response to the reduction of NOx emission by
470   50% (HalfNOx - CTL) show negative TRCO anomalies all over the globe (Fig. 3i). The global
471   mean TRCO anomalies are reduced by -3.7 [-7.9 to -1.1] ppb. Large decreases in TRCO
472   anomalies are seen over Arabia, South and East Asian regions (2.6 – 12.8 ppb). The TRCO
473   anomalies from HalfVOC - CTL show an overall decrease in TRCO by -0.27 [-0.97 to -0.4]
474   ppb (Fig. 3j). Further, a small enhancement is noted in the TRCO anomalies (by 0.5 – 1 ppb)
475   in the southern tropics and south polar region, while a decrease of -2.3 to 0.3 ppb is observed
476   in the NH. (Fig. 3j). Figure 3 clearly portrays that the TRCO response to NOx emission change
477   is larger than that of VOCs. There is a spatially distinct distribution in TRCO associated with
478   the region-specific ozone photochemical regimes (more discussion on the ozone photochemical
479   regimes will be detailed in sections 4 – 6).

480   **3.3. Spatial distribution of trends in ozone**

481   We estimate trends in TRCO from ECHAM CTL simulations (1998–2019) and OMI/MLS
482   satellite retrievals (2005–2019). The simulated trends are compared with satellite retrieves for
483   the period 2005–2019. Since IASI–GOME2 has a short observation period (2017–2019) and
484   IASI–SOFRID has negative drift in the SH, only TRCO from OMI/MLS is considered for trend
485   estimation (Fig. 4). The spatial pattern of trends from OMI/MLS shows fair agreement with
486   model simulations (Fig 4a-b). Quantitatively, the global mean TRCO trend from OMI/MLS is
487   slightly lower than the model (OMI/MLS:1.43 [-0.5 to 3.2] ppb decade^{-1}; ECHAM-CTL: 1.58
488   [0.3 to 3.3] ppb decade^{-1}). Both datasets reveal high trends, ranging from 3–4 ppb decade^{-1},
489   across regions such as South Asia, East Asia, and the West Pacific. OMI/MLS show negative
490   trends over parts of Africa, South America, Australia, and the southeastern Pacific (Fig. 4b),
491   which is not simulated in ECHAM6–HAMMOZ. Although there is fair agreement in spatial

492 patterns of TRCO trends between OMI/MLS and the model, the minor differences may be due

493 to the model's tendency to underestimate ozone levels and differences in the seasonal cycle. (See

494 Fig. 1).

495

496 TRCO trends analyzed from the Total Ozone Mapping Spectrometer (TOMS) indicate a

497 consistent absence of trend over the tropical Pacific Ocean, with notable positive trends ($4 - 5\%$

498 decade^{-1}) seen in the mid-latitude Pacific regions of both hemispheres (Ziemke et al., 2005).

499 This pattern is consistent across the ECHAM6–HAMMOZ and OMI/MLS data, although their

500 magnitude differs (Fig. 4 a–b). TOMS data also showed trends of ~$2 - 5\%$ decade^{-1} across

501 broad regions of the tropical South Atlantic, India, Southeast Asia, Indonesia, and the

502 tropical/subtropical regions of China during $1979 - 2003$ (Ziemke et al., 2005; Beig and Singh,

503 2007) which are also simulated in the model. Further, a large positive trend of ~2.5 ppb decade^{-1}

504 observed near $50°$ S in OMI/MLS is not simulated by the model (Fig. 4a–b). The CESM2–

505 WACCAM6 simulation from 1950 to 2014 also shows the largest trend estimate of 0.8 Tg

506 decade^{-1} over $20°$ N $- 30°$ N (Fiore et al., 2022). Large TRCO trends over $20°$ N $- 30°$ N are

507 also seen in OMI/MLS and the model (Fig.4). Wang et al. (2021) reported TRCO trends varying

508 between 2.55 to 5.53 ppb decade^{-1} during 1995–2017 over South and East Asia using IAGOS,

509 ozonesonde observations, and Goddard Earth Observing System–chemistry model (GEOS–

510 Chem). Our model also shows similar increasing trends.

511
512
513
514
515
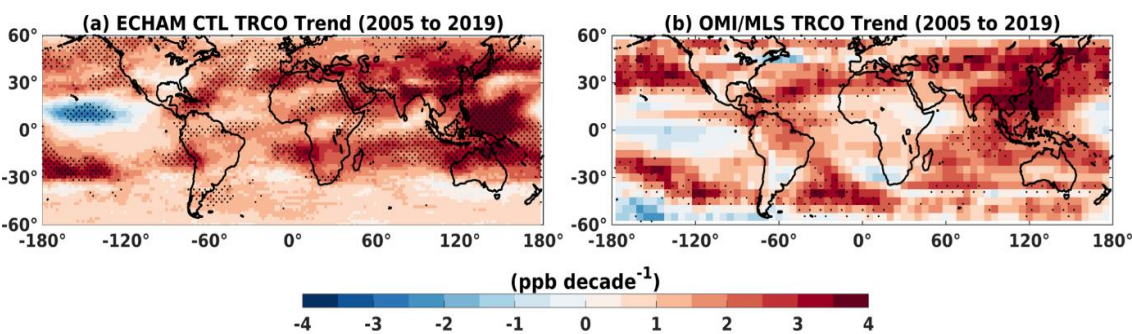
516 Figure 4. Trend of TRCO (ppb decade^{-1}) from (a) ECHAM CTL, and (b) OMI/MLS satellite
517 for the period January 2005 to December 2020. Stippled regions in the figures indicate trends
518 significant at 95% confidence based on the t-test.

519

520   Figure 5 shows the spatial distribution of estimated trends in surface ozone and TRCO

521 from CTL simulation for the period $1998 - 2019$. Changes (Doubling/halving) in the emission

of NOx and VOCs will change ozone trends. Hence, we also analyzed anomalies in ozone from DoubNOx - CTL, DoubVOC - CTL, HalfNOx - CTL, and HalfVOC - CTL. The surface ozone trend in the CTL simulation shows spatial variation with a pronounced increasing trend over South Asia and the Middle East (3 – 4 ppb decade^{-1}) (Fig. 5a). Similar pronounced increase is also seen in the TRCO trend (Fig. 5b). The estimated global mean TRCO trend from CTL is 0.89 [-0.07 to 2.1] ppb decade^{-1}. However, the negative trends in surface ozone over Mexico, certain parts of the US, and East China are barely discernible in the TRCO data. This discrepancy may stem from the interplay of mixing and transport processes, stratospheric intrusions, which are crucial when assessing ozone levels across the tropospheric column. The stratospheric ozone intrusions lead enhancement in the tropospheric ozone (Prather and Zhu, 2024).

Figure 5 c–d shows the trend in surface ozone and TRCO estimated from anomalies obtained from DoubNOx - CTL simulations. A striking feature is the large negative trend over India and China at the surface (-4.8 to -8 ppb decade^{-1}) and TRCO (-2 to -4 ppb decade^{-1}). Whereas Europe, the US, some parts of Africa and South America show positive trends at the surface (1.8 to 8 ppb decade^{-1}) and TRCO (2 to 4 8 ppb decade^{-1}). The global mean TRCO trend are 1.2 [-0.1 to 2.7] ppb decade^{-1}.

When global emissions of VOCs are doubled, the trend in ozone estimated from anomalies (DoubVOC - CTL) shows a decrease (by -0.8 to -1.9 ppb decade^{-1}) in surface ozone over Europe, Africa and some parts of the US, while strong positive trend (1.6 to 2 ppb decade^{-1}) are seen over India and China (Fig. 5e). TRCO trends show an enhancement over South Asia, Southwest Asia, China, parts of the Indian Ocean, and the western Pacific (0.8 to 1.6 ppb decade^{-1}) (Fig. 5f). A global mean TRCO trend for DoubVOC-CTL simulation is 0.5 [-0.03 to 1.04] ppb decade^{-1}. The estimated enhancement in global mean TRCO trend for DoubVOC is less than DoubNOx simulations. Figures 5 c and e also give indications of the existence of distinct ozone photochemical regimes globally. The increasing (decreasing) trend in surface ozone with an increase in VOC (NOx) over India and China indicates that these regions are in a VOC–limited regime, and vice-versa over the US and Europe indicates that these regions are in a NOx–limited regime (more discussions on sections 4 to 6).

553

554   Figure 5g–h shows the trend in surface and TRCO ozone estimated from anomalies

555   from HalfNOx - CTL. The surface ozone trend shows a large negative trend over Europe and

556   South Asia, while a positive trend over the US, China, and Australia (Fig. 5g). Trends in TRCO

557   also show a large negative trend over South Asia (Fig. 5h). Although anthropogenic NOx

558   emissions are halved compared to CTL, ozone trends are positive over large region globally.

559   Our investigations reveal that the trend in VOC anomalies from the HalfNOx-CTL simulations

560   is positive over the US, India, and Europe, while negative over China. Similarly, the trend in

561   NOx anomalies from the HalfNOx-CTL simulations is positive over the US and Europe while

562   negative over India and China (Fig. S1a-b). It should be noted that over the US and Europe the

563   positive NOx trend estimated from anomalies (HalfNOx-CTL) suggests that NOx levels in

564   HalfNOx are declining more slowly compared to CTL, leading to relatively higher NOx

565   concentrations over time. Meanwhile, over India and China, the NOx level is weak in HalfNOx

566   compared to CTL, leading to a negative trend estimated from NOx anomalies (HalfNOx-CTL).

567   It is known that ozone response is non-linear to NOx and VOC emission changes and

568   depends on the local photochemical regime. In the US, estimated trends from anomalies are

569   positive in VOC and NOx (HALFNOX-CTL). This indicates that relatively more ozone

570   precursors in the HalfNOx contribute to the observed positive ozone trend. Over Europe, the

571   strong positive trend estimated from NOx anomalies (compared to VOCs) enhances NOx

572   titration effects, contributing to the observed negative ozone trend. China, being a VOC–

573   limited regime, experiences reduced NOx titration under lower NOx conditions, resulting in

574   positive ozone trends. Over India, the positive trend in VOC anomalies with a negative trend

575   in NOx anomalies may enhance the radical destruction of ozone caused by aromatic

576   hydrocarbons in low NOx conditions (Taraborrelli et al., 2021), resulting in a negative ozone

577   trend. For HalfNOx – CTL, the global mean trend is positive 0.47 [-0.76 to 1.3] ppb decade^{-1}.

578

579   The trend in surface and TRCO ozone estimated from anomalies from HalfVOC – CTL

580   is shown in Figure 5i-j. A large negative trend in surface ozone is noted over IGP and China,

581   while an insignificant positive trend is noted over the US and Europe (Fig. 5i). The TRCO

582   trend are positive over large regions in the world with pronounced high over the mid- and high

583   latitudes although emissions of all anthropogenic VOCs are halved (Fig. 5j). The global mean

584   trend for HalfVOC - CTL is 0.37 [-0.35 to 1.02] ppb decade^{-1}. Our analysis shows that the

585   trend in NO$_X$ anomalies and VOC anomalies from HalfVOC - CTL is decreasing over both

586   India and China (Fig S1c-d). The negative trend in precursors might have resulted in a negative

587   trend in ozone over these regions. The absence of strong trends in TRCO (Fig. 5 b, d, f, h, j)

588   similar to that at the surface (Fig. 5 a, c, e, g, i) in all the simulations indicates the potential

589   contribution of transport in the troposphere and stratospheric intrusions in TRCO. Ozone

590   injection through stratosphere–troposphere exchange is important source of tropospheric ozone

591   (Prather and Zhu, 2024).

592
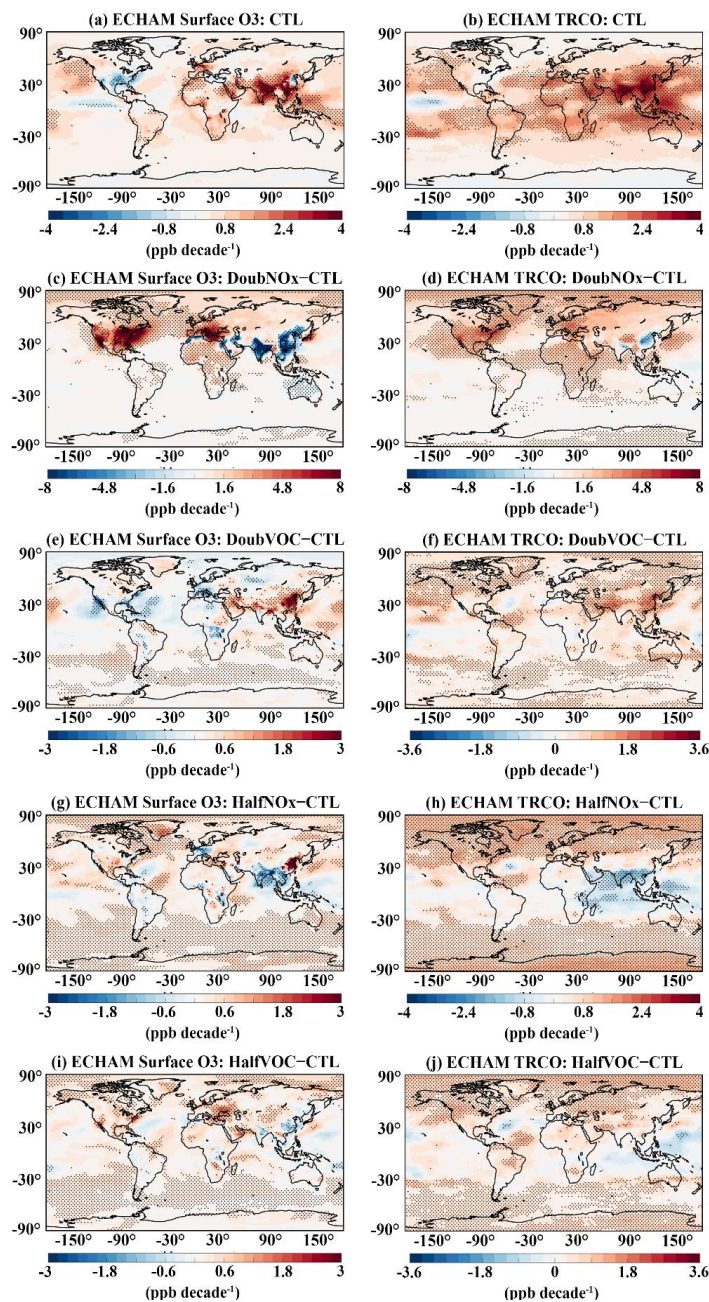
Figure 5. Trend in surface ozone (ppb decade^{-1}) for the period 1998-2019, calculated from (a) CTL, ozone anomalies in (c) DoubNOx - CTL, (e) DoubVOC - CTL, (g) HalfNOx - CTL, and (i) HalfVOC - CTL simulations. Panels (b, d, f, h, and i) represents the corresponding trend in TRCO. The stippled regions in the figures indicate significance at 95% confidence based on the t-test.

3.4. Trends in emission and tropospheric column of NO$_2$ and HCHO

We show mean emissions of NOx (NO+NO$_2$) and HCHO over urban/semi-urban regions; US, Brazil, Europe, Africa, India, China, and Australia in Figure 6. High emissions of VOCs and NOx in India and China are evident in Figure 6. Furthermore, VOCs emissions are noted to be higher than NOx over all the regions. They are higher by a factor of 3.3 in the US, 11.3 in Brazil, 4.8 in Europe, 10.5 in Africa, 10.8 in India, 6.1 in China, and 6.7 in Australia.
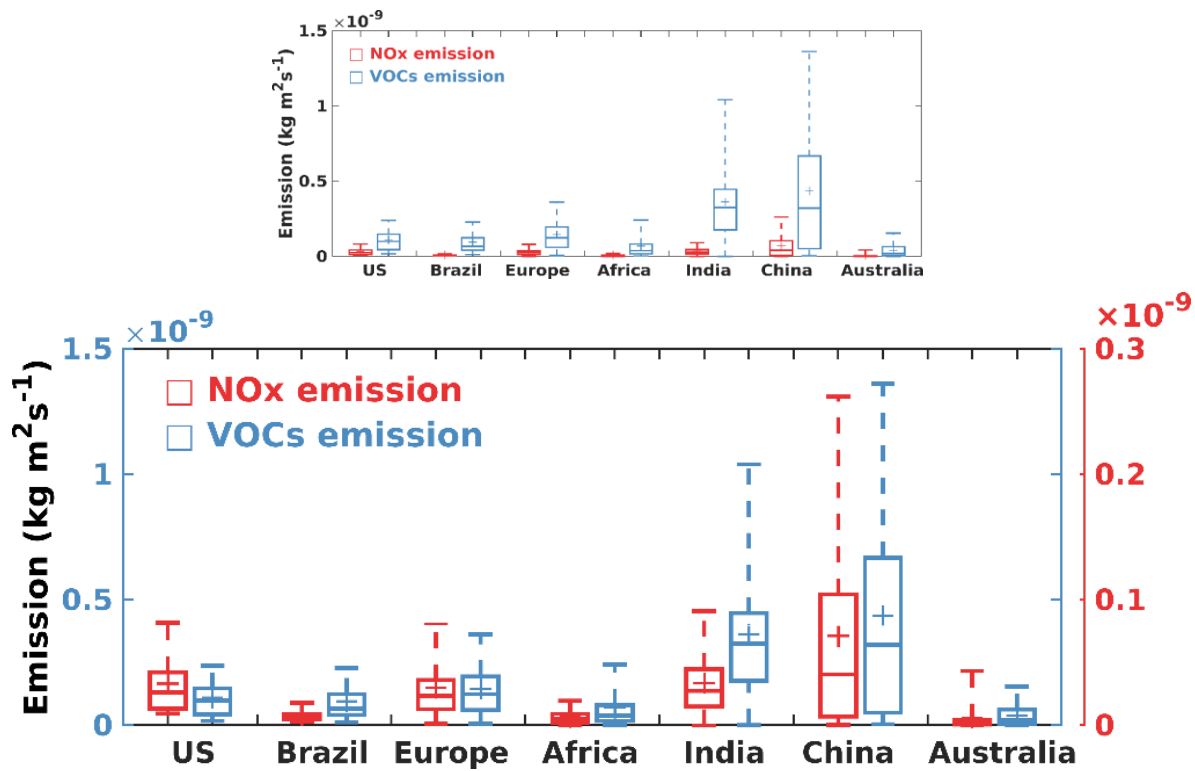
Figure 6. Box and whisker plot illustrating the NOx (NO+NO$_2$) and VOCs emission over the regions US (85°W – 110°W, 35°N – 44°N), Brazil (34°W – 49°W, 24°S – 3°S), European Union (9°W – 45°E, 35°N – 55°N), Central Africa (14°W – 45°E, 0° – 14°N), India (75°E – 90°E, 8°N – 30°N), China (110°E – 125°E, 30°N – 42°N), and South Australia (134°E – 154°E, 38°S – 28°S) from the ECHAM model. The box represents the 25 and 75 percentiles, and the whisker represents the 5 and 95 percentiles. The plus marker represents the mean, and the horizontal bar represents the 1 and 99 percentiles.

647   The trends in ozone are partly modulated by the change in the emission of its precursors and

648   partly by meteorology (e.g., Verstraeten et al., 2015). We show trends in emissions and

649   tropospheric column amounts of ozone precursors NO_2 and HCHO from ECHAM CTL and

650   OMI satellite retrievals in Figure 7. NO_2 and HCHO are considered here because column

651   densities of these will be used to identify the ozone photochemical regimes discussed later in

652   Sections 4–6. Emissions and tropospheric columns of HCHO and NO_2 from ECHAM–CTL

653   show large positive trends over the South and East Asian regions (Fig. 7a–d). These regions

654   show large positive ozone trends in both model and OMI satellite data (see Fig. 4 and 5). Over

655   Europe and the US, the emission trend in both HCHO and NO_2 from the model is negative

656   (Fig. 7a, c). Though a similar negative trend in tropospheric column NO_2 is seen over these

657   regions, a marginal positive trend is noted for HCHO (Fig. 7b, d). The positive trend in column

658   HCHO could be due to secondary production pathways from biogenic emissions or methane

659   oxidation and transport (e.g., Anderson et al., 2017; Alvarado et al., 2020). The positive trend

660   in ozone (Fig. 4a–b and 5a, f) along with a negative trend in NO_2 and HCHO (Fig. 7a–d) over

661   Europe indicates that ozone production over this region has been initially controlled by VOCs

662   (i.e., VOC–limited regime; detailed discussed in section 4). However, a large decreasing trend

663   in NO_2 compared to that of HCHO over this region might have decreased the NOx titration

664   effect, resulting in an increase in ozone. On the contrary, a negative trend in surface ozone (Fig.

665   5a) along with negative trends in NO_2 and HCHO are seen over the US (Fig. 7a–b). The

666   decrease in both NO_2 and HCHO would have resulted in a decreasing trend in surface ozone

667   over this region. This also indicates that the US might have been in a NOx–sensitive regime

668   before and the large negative trend in NO_2 might have resulted in the decreasing trend in ozone

669   (discussed further in section 4-6).

670

671   Further we compared the simulated trends in column HCHO and NO_2 with the OMI retrievals

672   for the period 2005–2019 (Fig. 7e–h). OMI shows a positive trend in tropospheric column

673   HCHO over South Asia ($1 - 1.5 \times 10^{15}$ molecules cm^{-2} $decade^{-1}$), parts of western China (0.75

674     $- 1.25 \times 10^{15}$ molecules cm^{-2} $decade^{-1}$), the Iranian Plateau ($0.5 - 1 \times 10^{15}$ molecules cm^{-2}

675     $decade^{-1}$), the Amazon ($1 - 1.5 \times 10^{15}$ molecules cm^{-2} $decade^{-1}$), North America ($0.5 - 1.5$

676     $\times 10^{15}$ molecules cm^{-2} $decade^{-1}$), Europe ($0.5 - 1 \times 10^{15}$ molecules cm^{-2} $decade^{-1}$), and central

677   Africa ($1 - 1.5 \times 10^{15}$ molecules cm^{-2} $decade^{-1}$). The model simulated trends show reasonable

678   agreement with OMI, except for western areas in central Africa, north Africa, southwest and

southeast China, and some parts of Australia. Over these regions OMI indicates a negative trend, while the model suggests a marginal positive trend. OMI and ECHAM CTL show a good agreement in the tropospheric column NO_2 trend. Both datasets show negative trends over the eastern US and Europe, and positive trends over the Middle East, and South Asia. However, differences are seen in eastern China and central Africa, where OMI indicates a negative trend, while the model shows a strong positive trend. The differences between simulated and OMI HCHO and NO_2 column trends may be due to sampling time and differences in seasonal cycle. Figures 4, 5, and 7 clearly indicate the impact of ozone precursors on the spatial distribution of ozone trends. This warrants a detailed discussion on the spatial distribution of ozone precursors and their impact on ozone production-sensitive regimes, which will be presented in the next section.
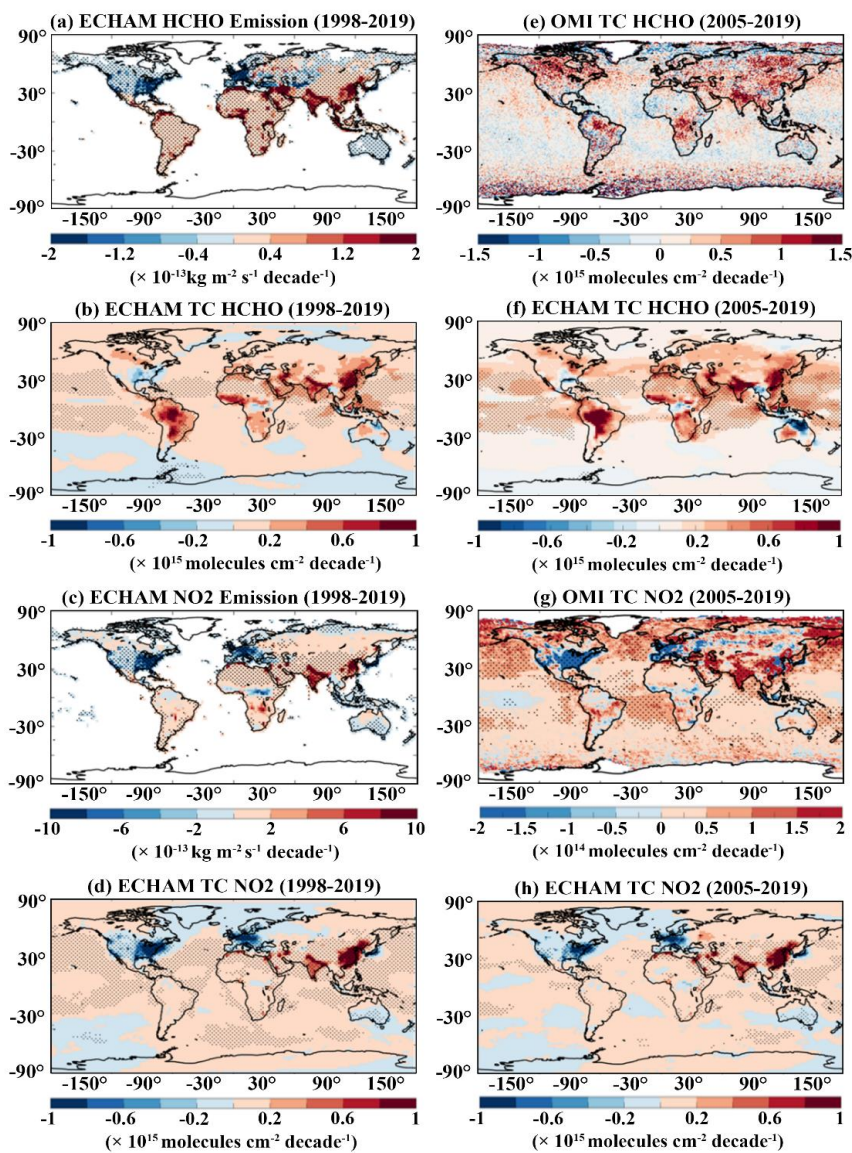
Figure 7. Trend in anthropogenic emission (kg m^2 s^{-1} decade^{-1}) from ECHAM CTL simulation for the period 1998–2019 for (a–b) HCHO and NO$_2$ respectively. Trends in tropospheric column (TC) (molecules cm^{-2} decade^{-1}) for (c–d) HCHO and NO$_2$ respectively. Trend in tropospheric column of HCHO from (e) OMI, and (f) ECHAM–CTL simulations for the period 2005-2019. (g–h) are the same as that of (e–f) but for tropospheric column NO$_2$. The stippled regions in the figures indicate significance at 95% confidence based on the t–test.

4. Influence of NOx and VOCs emissions on Formaldehyde to Nitrogen dioxide Ratio

In this section, we diagnosed the spatial distribution of tropospheric ozone production sensitivity regimes (NOx–limited/VOC–limited) associated with simulations of emission changes by using formaldehyde to nitrogen dioxide ratio (FNR). We estimate the FNR thresholds from ECHAM6–HAMMOZ model simulations adhering to the methodology outlined by Jin et al. (2017). The procedure to obtain FNR threshold from monthly mean data involves two steps: (1) obtaining the ~~annual and seasonal~~ ozone response from emission sensitivity simulations (here, HalfNOx and HalfVOC simulations) by considering only the polluted cells over the study region and plotting it as a function of FNR (Fig. 8a), (2) calculating cumulative probability from this data for the conditions d[O$_3$]/dE$_{NOx}$ < 0) (VOC limited) and (d[O$_3$]/dE$_{NOx}$ > d[O$_3$]/dE$_{VOC}$ > 0) (NOx–limited) (Fig. 8b), where d[O$_3$]/dE represents the change in ozone corresponding to a change in emission of either NOx or VOCs. This approach is applied to estimate ~~seasonal and annual~~ FNR thresholds to distinctly delineate the ozone photochemical regimes as NOx or VOC–limited over major urban and semi-urban regions. The regions considered for estimating the FNR are shown in Figure 9.
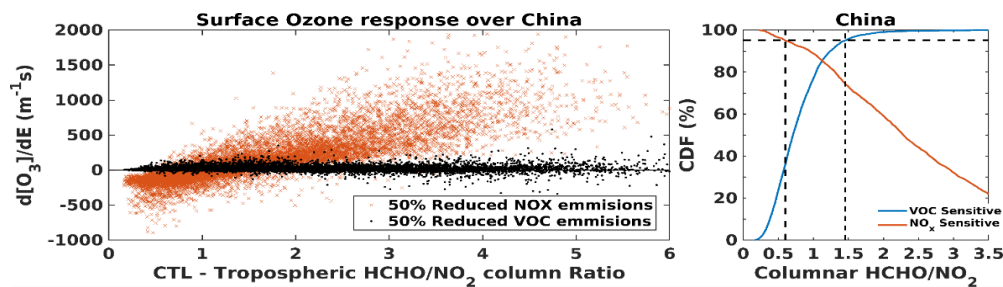
Figure 8. (a) Typical example of a normalized surface ozone sensitivity to a 50% reduction in global NOx (HalfNOx) and VOC (HalfVOC) emissions versus tropospheric column HCHO/NO$_2$ ratio derived from ECHAM6–HAMMOZ model simulation over China for the period 1998 – 2019, (b) Cumulative probability (CP) of VOC–sensitive (d[O$_3$]/dE$_{NOx}$ < 0) and NOx–sensitive (d[O$_3$]/dE$_{NOx}$ > d[O$_3$]/dE$_{VOC}$ > 0) conditions, as a function of tropospheric column HCHO/NO$_2$ as simulated by the ECHAM6–HAMMOZ model. The horizontal dashed line represents the 95% CP, and the vertical dashed lines represent the HCHO/NO$_2$ ratio corresponding to 95% CP for both the VOC–sensitive and NOx–sensitive curves demarcating the VOC–sensitive, NOx–sensitive, and transition regimes.
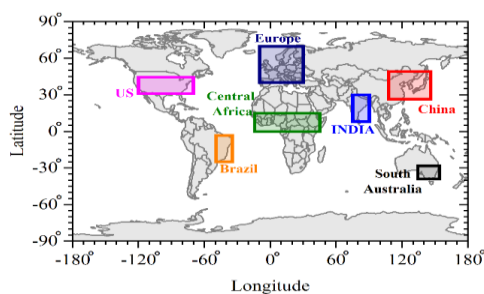
Figure 9. The rectangular box marks indicate the regions considered for estimating the HCHO/NO$_2$ ratio (FNR).

Table 3 presents FNR thresholds across the regions outlined in Figure 9. Based on ECHAM6-HAMMOZ simulations, our analysis closely mirrors the threshold ranges documented in prior research. For instance, during summer in the USA, many studies report FNR thresholds within the 0.8 – 2 range (Chang et al., 2016; Jin et al., 2017; Roberts et al., 2022), while our simulations indicate a range of 0.3 to 1.05. Similarly, across China, previous studies have reported FNR thresholds spanning 1 – 2 (Lee et al., 2022) and 0.6 – 3 (Chen et al., 2023), aligning closely with our simulated range of 0.6 – 1.45. It is interesting to note that the transition region exhibits a very narrower range in the US, Europe, and China, indicating that the transition from VOC-limited to NOx-limited can happen suddenly in response to changes in the emission of NOx/VOC. Whereas the transition region is wider in Central Africa.

Table 3. Estimated values of the tropospheric HCHO/NO$_2$ columns threshold ratios from ECHAM6-HAMMOZ model control simulation to identify the NOx and VOC sensitive regimes across various regions. The FNR less than the lower limit indicates VOC-limited, and that higher than the upper limit indicates NOx-limited regimes.

Sr. No.	Regions	Transition limits	
1	US (85° W – 110° W, 35° N – 44° N)	0.44	1.14
2	Brazil (34° W – 49° W, 24° S – 3° S)	3.04	7.53
3	European Union (9° W – 45° E, 35° N – 55° N)	0.3	1.37
4	Central Africa (14° W – 45° E, 0° – 14° N)	3.24	7.19
5	India (75° E – 90° E, 8° N – 30° N)	2.27	4.63
6	China (110° E – 125° E, 30° N – 42° N)	1.14	1.91
7	South Australia (134° E – 154° E, 38° S – 28° S)	1.03	3.28

Further, we compared the model-estimated FNR with the OMI-derived FNR for the period 2005 – 2019. Figure 10 illustrates the comparison of FNR estimated from ECHAM6–HAMMOZ CTL simulations with OMI. The spatial map of FNR shows fairly good agreement between OMI and the model. Over the urbanized regions (e.g., South Asia, Europe, the US, and China) both the model and OMI show FNR < 4. In contrast, regions like North Canada, South America, central Africa, Australia, and Siberia exhibit high FNR values >9. There is good agreement between the model simulations and OMI, however, some minor differences are seen between the model and OMI FNR over the west coast of South America, South Africa, the Tibetan Plateau, and western Australia.
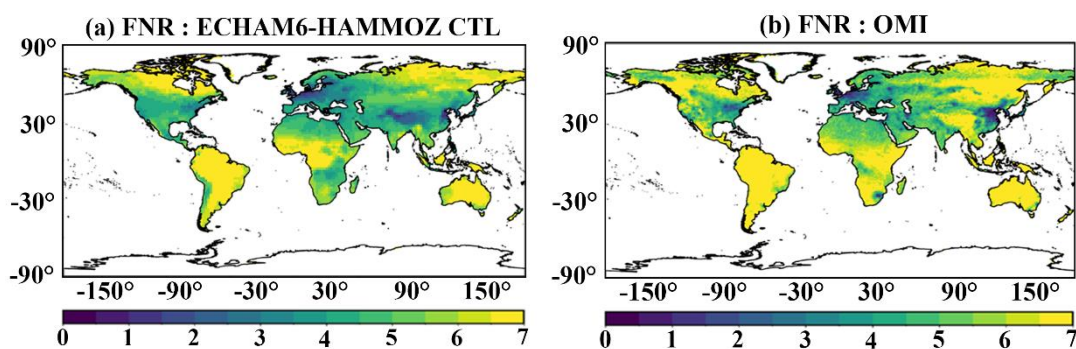
Figure 10. Spatial distribution of mean tropospheric column HCHO/NO$_2$ (FNR) obtained from ECHAM6–HAMMOZ CTL simulations (2005 – 2019) and OMI (2005 – 2019).

These differences could be due to the underestimation of HCHO in the model over these regions. Considering the fair performance of the model in comparison with OMI, we further analyzed the influence of changes in NOx and VOC emissions on the FNR from the model simulations, which are discussed in the subsequent sections.

Figure 11 shows the spatial distribution of FNRs estimated from CTL, DoubNOx, DoubVOC, HalfNOx, and HalfVOC simulations. In the control simulation for the period 1998 – 2019, most of the polluted cities/industrialized areas in the US, Canada, Europe, west Russia, East China, Korea and Japan are VOC limited (FNRs <2). The NOx–limited regimes (largest FNR values >5) are found over the rural or unpolluted background regions like tropical rainforest, savanna, and arid climates where biogenic emissions of VOCs are high (e.g., Millet et al., 2008; Shen et al., 2019) (see Table 3 and central Africa in Fig. 11f). The DoubNOx simulation yields

5. Seasonal variation of Formaldehyde to Nitrogen dioxide Ratio

Since the emission of HCHO and NO_2 varies with the seasons across the globe (e.g., De Smedt et al., 2015; Wang et al., 2017; Surl et al., 2018; Kumar et al., 2020; Goldberg et al., 2021; Guan et al., 2021), understanding the seasonal changes in FNR is ~~also~~ crucial for comprehending shifts in ozone photochemical regimes. In this regard~~, using the methodology described in Section 4~~, we extracted the seasonal changes in transition limits for the major urban and semi-urban regions shown in Figure 9 and summarized in Table 43. Figure 112 illustrates the seasonal variation of estimated FNR from both OMI data and model simulations across these key urban regions. In general, all regions exhibit distinct seasonal variations in transition limits (Table 43). Previously reported transition limits over the US (2 – 5: Johnson et al., 2024; 1.1 – 4: Schroeder et al., 2017) and China 0.6 – 1.5/1.25 – 2.39 (Chen et al., 2023) during the summer season are also compared with our model estimates. The estimated FNR values from the ECHAM6–HAMOZ simulations show fair agreement over both locations (0.4 – 4.6 in the US and 0.58 – 2.56 in China) with some minor differences. These minor discrepancies in the estimated FNR could be due to differences in the chosen location, time period and dataset used. Chen et al. (2023) have also reported that the transition limits depend on the region considered for the analysis.

Based on the threshold values depicted in Table 34 and the mean FNR in Figure 112, the seasonal change in ozone photochemical regimes over the key regions associated with the different emission scenarios are assessed. In the CTL simulation (Fig. 112e – h), the US,

Europe, and China are found to be in the transition regime, while all other regions are NOx–limited during winter. In spring, every region except India remains NOx–limited, with India transitioning into the transition regime. During summer and autumn, all regions shift to a NOx–limited condition. We further compared the model-estimated regional FNR from the CTL simulation with the OMI-derived FNR shown in Figure 112a – d. The ozone photochemical regimes inferred from both OMI and the model show consistent results except during winter. During winter, the US, Europe and China are NOx limited in OMI, while our model shows them in the transition regimes.

Doubling NOx (DoubNOx) leads to a shift to a VOC–limited regime in all regions except Africa and Australia during winter, spring, and autumn (Fig 112i – l). The relatively high VOC contributions in Africa and Australia likely keep these regions in the transition regime. During summer, the US, Europe, Africa and Australia transform to the transition regimes, while all other regions remain VOC–limited. In both the DoubVOC and HalfNOx scenarios (Fig 112m – t), ozone photochemical regimes show no seasonality. All regions consistently exhibit a NOx–limited regime throughout all seasons. In the HalfVOC simulation (Figure 112u – x), the US, Europe, and China are in transition regimes, while all other regions become NOx–limited during winter. India remains in a transition regime during all other seasons, whereas other regions consistently exhibit NOx–limited conditions. Figure 11 also depicts that DoubNOx and HalfNOx simulations greatly impact the shift in ozone photochemical regimes compared with DoubVOC and HalfVOC simulations. This indicates that ozone photochemistry is highly sensitive to changes in NOx emissions globally.

Table 34. Seasonal mean estimated values of the tropospheric $HCHO/NO_2$ columns threshold ratios from ECHAM6–HAMMOZ model control simulation to identify the NOx and VOC sensitive regimes across regions mentioned in Figure 9. The FNR less than the lower limit indicates VOC–limited, and that higher than the upper limit indicates NOx–limited regimes.

Sr. No.	Regions	Transition limits of FNR							
		DJF		MAM		JJA		SON	
1	US	0.48	1.04	0.49	1.15	0.49	4.69	0.45	1.39
2	Brazil	2.93	7.79	2.93	6.66	2.93	6.02	3.12	8.44
3	European Union	0.33	1.13	0.33	1.17	0.33	3.32	0.3	1.45
4	Central Africa	2.95	7.26	2.92	5.66	2.93	6.56	3.14	7.06
5	India	2.23	3.91	2.22	9.19	2.22	5.76	2.27	5.29
6	China	0.56	1.85	0.57	1.86	0.58	2.56	1.14	2.01
7	South Australia	1.1	5.54	1.09	2.3	1.09	1.82	1.12	3.93
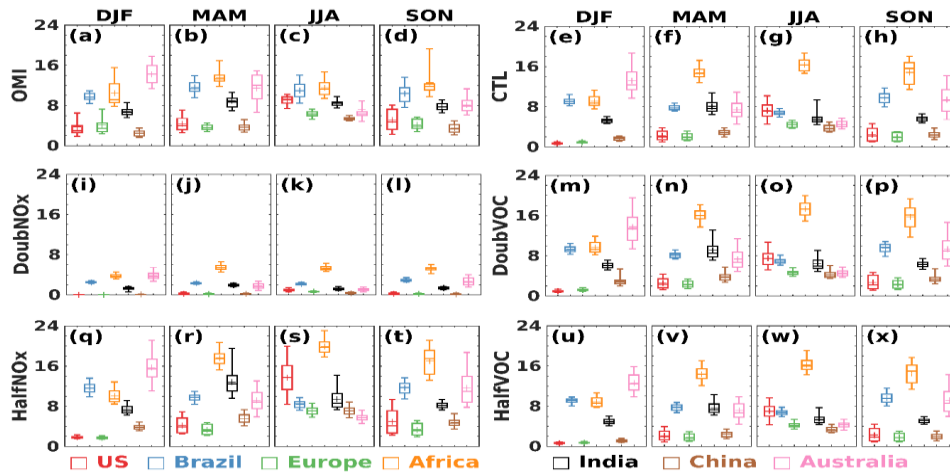
Figure 1 12. Box and whisker plot illustrating the long-term seasonal average FNR over the regions depicted in Fig.7 from (a-d) OMI observations, and model (e-h) CTL, (i-l) DoubNOx, (m-p) DoubVOC, (q-t) HalfNOx, and (u-x) HalfVOC simulations. Box represents 25 and 75 percentile and whisker represents 5 and 95 percentiles. The plus marker represents the mean, and the horizontal bar represents the 1 and 99 percentiles.

5 6. Influence of NOx and VOCs emissions on trends of Formaldehyde to Nitrogen dioxide Ratio

Trend analysis is carried out on FNR to understand the temporal evolution of ozone photochemical regimes associated with different emission scenarios. Figure 1 23 illustrates trends of FNR during the period 1998 – 2019 from CTL, DoubNOx, DoubVOC, HalfNOx, and HalfVOC simulations. In CTL simulation, decreasing (negative) trends in FNR are seen over the Asian region (-0.4 to -1.2 decade^{-1}) and Australia (-0.8 to -1.6 decade^{-1}), and an increasing (positive) trend in Europe (0.2 decade^{-1}) and the US (0.8 – 1.4 decade^{-1}) (Fig. 1 23a). These

observed trends in FNR are mainly driven by the region-specific trends in HCHO and NO_2 (Fig. 7). Figure 7 shows a higher positive trend in NO_2 than in HCHO in the Asia region, causing an overall decreasing trend in FNR, indicating a tendency towards VOC–limited regimes. Whereas, over the US and Europe, there is a higher negative trend in NO_2 than HCHO, causing a positive trend in FNR, indicating a tendency towards a NOx–limited regime. A recent study by Elshorbany et al. (2024) also reported a significant positive trend over Europe and the US and a negative trend over Asia using the OMI-based tropospheric column HCHO/NO_2 ratio. Further, long-term column measurements of HCHO and NO_2 from OMI over India and China have revealed an increasing trend in NO_2 compared to that of HCHO, causing a decreasing trend in FNR over these regions (Jin and Holloway, 2015; Mahajan et al., 2015).

DoubNOx simulation (Fig. 123b) shows a similar spatial trend pattern to that of CTL simulation (Fig. 123a). However, the magnitude of this trend is less than that of the CTL. For example, a weak positive trend is noted in the US and Europe ($0.2 - 0.4$ decade^{-1}), while trends over India, and China are less negative (-0.2 to -0.4 decade^{-1}) in DoubNOx than CTL. (Fig. 123b). On the contrary, the magnitude of the positive trend over Canada and the negative trend over central Africa increased in DoubNOx emission, while the negative trend over Australia became nominal and insignificant. This indicates that Canada and central Africa have a tendency to become NOx–limited and VOC–limited respectively.

In DoubVOC simulations, trends are marginally increasing over the US, Canada, and Europe compared to the CTL (Fig. 123a and 123c). A notable change is observed over the Middle East and Amazon, where trends become more negative and positive respectively compared to CTL. The negative trends over Australia in the CTL become nominal and insignificant in the DoubVOC simulation. In HalfNOx simulations (Fig. 123d), the positive trends are higher over the US, Europe and Amazon, while negative trends prevail over India, China and northeast Australia. Meanwhile, in HalfVOC simulation, marginal changes are noted globally compared to CTL. The most pronounced change in the FNR trend is observed over West Australia, where the negative trend in CTL becomes positive in HalfVOC (Fig. 123e). Figure 123f clearly shows that the trend in FNR is always negative over India and China for all the simulations, indicating that these regions have a tendency to become VOC–limited, while the positive trends over Europe and US show a tendency to become more NOx–limited. Further, from Figures 5, 11 and 123, we can infer that the relation between trends in FNR and ozone exhibits a nonlinearity.

969 For example, even though FNR shows a negative trend over India and China for all the
970 simulations, the TRCO trend depends on the specific emission scenario.

971
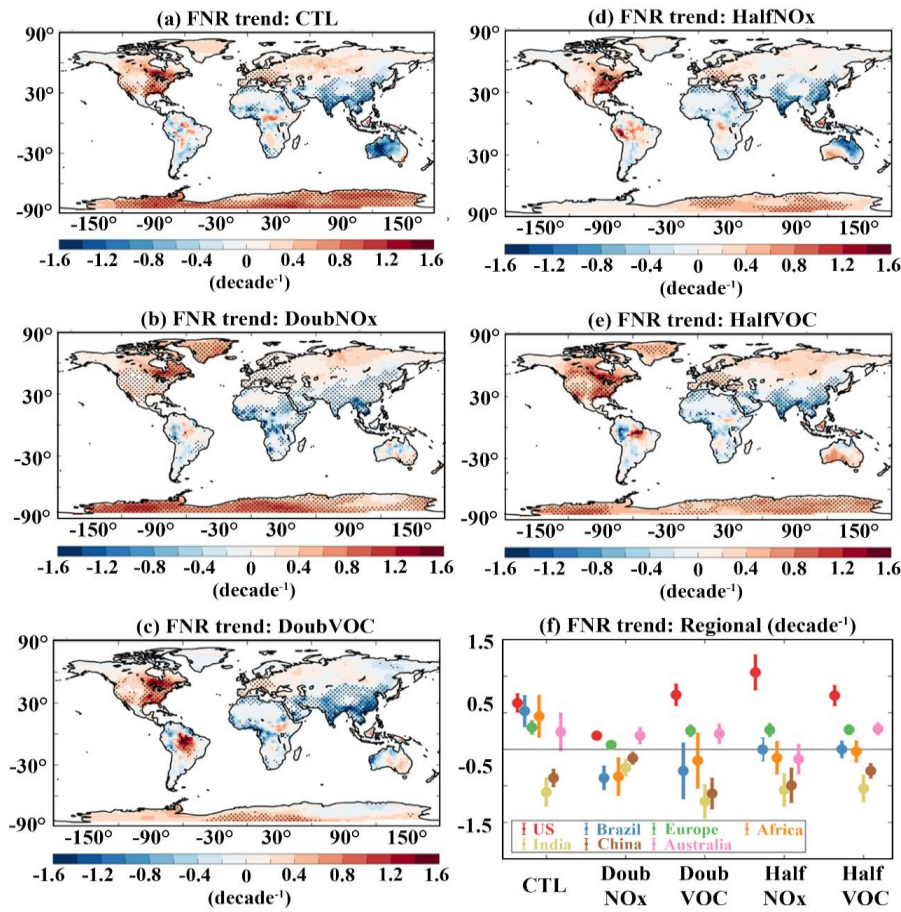
985 Figure 123. Trends in the tropospheric column HCHO/NO$_2$ ratio during 1998 – 2019 from
986 ECHAM6–HAMMOZ simulations for (a) for CTL, (b) DoubNOx, (c) DoubVOC, (d)
987 HalfNOx, (e) HalfVOC simulations. The stippled region indicates the trend significant at 95%
988 confidence based on the t-test. (f) scatter plot illustrating the long-term trend and standard
989 deviation over the regions depicted in Fig.9.

990

67. Tropospheric ozone radiative effects

992 The impact of emission changes on the tropospheric ozone radiative effect (TO3RE) is
993 estimated using the ECHAM6 model output and a radiative kernel method (see data and model
994 experiments). The estimated TO3RE for different model simulations are shown in Figure 134.
995 In the CTL simulations (Fig. 134a), the estimated global mean area-weighted average TO3RE
996 for the period 1998 to 2019 is 1.21 [1.1 to 1.3] W m^{-2}. High TO3RE is noted over North Africa
997 and the Middle East region in NH (~2.2 W m^{-2}), while in SH, it is over Australia and South

998 Africa (~1.2 W m^{-2}). TO3RE estimates from TES measurements (2005 – 2009) also show a

999 peak of 1.0 W m^{-2} in northern Africa, the Mediterranean, and the Middle East in June–July–

1000 August (Bowman et al. 2013). Recently, Pope et al. (2024) reported TO3RE estimates from

1001 IASI–SOFID, IASI–FORLI, and IASI–IMS for the period 2008 – 2017. The values reported

1002 by Pope et al. (2024) are comparable with our CTL simulation (e.g. IASI–FORLI: 1.23 W m^{-2},

1003 IASI–SOFRID: 1.21 W m^{-2}, IASI–IMS: 1.21 W m^{-2}, ECHAM6: 1.22 W m^{-2}).

1004

1005 The anomalies of TO3RE from DoubNOx-CTL simulations are shown in Figure 134b.

1006 Doubling of NOx emission causes an enhancement in TO3RE by 0.36 [0.23 to 0.5] W m^{-2}

1007 compared to the CTL simulation. It shows a peak over the Middle East and adjacent North

1008 Africa (0.7 W m^{-2}). A similar peak over this region is also seen in the CTL simulation.

1009 Doubling of VOC emissions causes a marginal decrease in global mean TO3RE by -0.005 [-

1010 0.05 to 0.04] W m^{-2}. TRCO enhancement for doubling NOx is also higher than doubling VOC

1011 (see Fig.3). DoubVOC-CTL simulations (Fig. 134 c) show a peak over the Arctic (0.02 W

1012 m^{-2}). The TO3RE anomalies are negative between 30° N – 30° S. These negative anomalies

1013 in TO3RE between 30° S – 30° N (Fig. 134c) can be attributed to negative anomalies of TRCO

1014 (Fig. 3h).

1015 The reduction of NOx emission by 50% reduced global mean TO3RE by -0.12 [-0.2 to -0.05]

1016 W m^{-2} than CTL. The anomalies in TO3RE from HalfNOx-CTL simulations (Fig. 134d) show

1017 negative anomalies all over the globe, with a strong decrease over the Middle East and adjacent

1018 North Africa (-0.25 W m^{-2}). Figures 134b and 134d show that the effect of

1019 enhancement/reduction of NOx emission is high over the Middle East and adjacent North

1020 Africa. The reduction of VOC emission by 50% reduced global mean TO3RE by -0.03 [-0.07

1021 to 0.02] W m^{-2} than CTL simulations (Fig. 134e). HalfVOC - CTL simulations show negative

1022 anomalies of TO3RE between 40° S – 40° N and positive 0.015 W m^{-2} (low confidence) over

1023 mid-high latitudes in NH and SH. From Figure 134, it is interesting to note that the magnitude

1024 of TO3RE and its response to emission change is pronounced over the Middle East compared

1025 to all other regions. Further, Figure 134f depicts the latitude variation of zonal mean TO3RE

1026 for different sensitivity simulations. It is clear from Figure 134f that the TO3RE response to

1027 emission change is large at the northern and southern mid-latitudes, around ±30°. Also, Figure

1028 134f clearly indicates that the impacts of NOx emission changes are larger than VOCs
1029 throughout the latitude band.
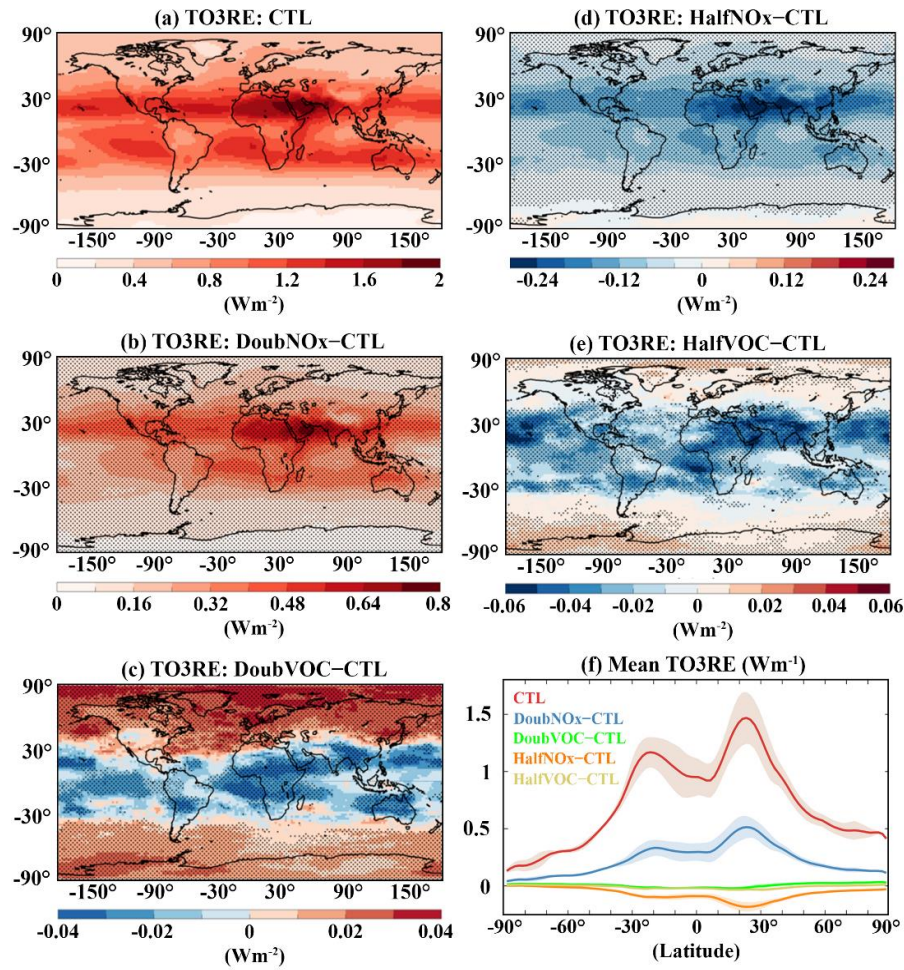
1045 Figure 134. Tropospheric Ozone radiative effects (TO3RE) (W m^{-2}) for (a) CTL, and
1046 anomalies from (b) DoubNOx - CTL, (c) DoubVOC - CTL, (d) HalfNOx - CTL, (e) HalfVOC
1047 - CTL simulations. Stippled regions in Figures (b–e) indicate TO3RE significant at 95 %
1048 confidence level based on the t-test, (f) line plot for zonal mean TO3RE (W m^{-2}) from CTL,
1049 DoubNOx - CTL, DoubVOC - CTL, HalfNOx - CTL, HalfVOC - CTL, shades indicate
1050 standard deviation.

1051

1052 **78 Summary and Conclusions**

1053 In this study, we report variation of tropospheric ozone levels, trends, photochemical regimes
1054 and radiative effects using the state-of-the-art ECHAM6–HAMMOZ chemistry-climate model
1055 simulations from 1998 to 2019. The model simulations are validated against multiple satellite
1056 observations. Our analysis shows that

1057 1. The estimated global mean trend in TRCO from CTL simulations for the period 1998 –
1058   2019 is 0.89 [-0.07 to 2.1] ppb decade^{-1}. Trend estimates from OMI/MLS (1.43 [-0.5 to
1059   3.2] ppb decade^{-1}) for the period January 2005 to December 2019 show good agreement
1060   with CTL (1.58 [0.3 to 3.3] ppb decade^{-1}) for the same period.

1061 2. TRCO anomalies from DoubNOx - CTL simulations show positive trends over Europe, the
1062   US, Africa, and South America, with a global mean trend of 1.2 [-0.1 to 2.7] ppb decade^{-1}.
1063   However, India and China show decreasing TRCO trend -2 to -4 ppb decade^{-1}. Surface
1064   ozone anomalies over these regions show strong negative trends -4.8 to -8 ppb decade^{-1}.

1065 3.   Global mean TRCO trend anomalies from DOUBNOX - CTL simulation is 1.2 [-0.1 to
1066   2.7] ppb decade^{-1}, while for DoubVOC - CTL is 0.5 [-0.03 to 1.04] ppb decade^{-1}. Global
1067   mean TRCO trend anomalies from HalfNOx - CTL is 0.47 [-0.76 to 1.3] ppb decade^{-1} and
1068   for HalfVOC - CTL is 0.37 [-0.35 to 1.02] ppb decade^{-1}.

1069 4. The spatial distribution of TRCO anomalies shows that enhancement is nearly 12 times
1070   higher in DoubNOx - CTL than in DoubVOC - CTL simulations. The largest increase in
1071   surface ozone anomalies from DoubVOC - CTL is observed over Indo-Gangetic Plains,
1072   Eastern China and the eastern United States (4 – 6 ppb), where a decrease in surface ozone
1073   anomalies is observed in the DoubNOx - CTL simulation. This decrease (increase) in ozone
1074   with an increase in NOx (VOC) indicates that these regions are VOC-limited.

1075 5. ~~The FNR shows that the transition from VOC-limited to NOx-limited happens suddenly~~
1076   ~~in response to changes in the emission of NOx/VOC over the US and China. Whereas this~~
1077   ~~transition region shows a wider range in Central Africa. Most polluted cities/industrialized~~
1078   ~~areas in the US, Canada, Europe, west Russia, East China, Korea and Japan are identified~~
1079   ~~with a low FNR, indicating VOC-limited (FNRs <2). Meanwhile, NOx-limited regimes~~
1080   ~~(largest FNR values >5) are primarily found in tropical rainforests, savannas, and arid~~
1081   ~~climates.~~

1082 ~~5.~~6. The FNR transition thresholds exhibit pronounced seasonal variability. In the CTL
1083   simulation, the US, Europe, and China remain in the transition regime during winter, while
1084   other regions are predominantly NOx-limited. In spring, NOx-limited conditions persist
1085   across all regions except India. A widespread shift to NOx-limited regimes is observed
1086   during summer and autumn.

7. ~~The DoubNOx simulation shows a notable change in the spatial extent of VOC limited regimes, particularly in the NH. While the SH exhibits minimal change in the spatial extent of VOC limited regimes.~~

~~6.~~8. The DoubNOx simulation indicates a consistent shift toward VOC-limited regimes across most regions, except Africa and Australia, during winter, spring, and autumn. In summer, VOC-limited conditions prevail in most regions, whereas the US, Europe, Africa, and Australia are in a transition regime.

9. ~~DoubVOC simulations reveal persistent VOC limited regimes over Western Europe, with moderate FNR values indicating a transition to NOx limited regimes across most of the NH. Comparing CTL and HalfNOx simulations globally shows a shift from VOC to NOx limited regimes.~~

~~7.~~10. In both the DoubVOC and HalfNOx scenarios all regions consistently exhibit a NOx–limited regime throughout all seasons. In the HalfVOC simulation the US, Europe, and China are in transition regimes, while all other regions become NOx–limited during winter. India remains in a transition regime during all other seasons, whereas other regions consistently exhibit NOx–limited conditions.

~~8.~~11. Comparison of all the emission simulations, DoubNOx and HalfNOx simulations influence the shift in tropospheric ozone photochemical regimes compared to DoubVOC and HalfVOC simulations, highlighting the global sensitivity of ozone photochemistry to NOx emissions changes.

~~9.~~12. Trends estimated from modelled FNR are negative over India (-0.6 decade^{-1}) and China (-0.4 decade^{-1}) in all the simulations, indicating that these regions have a tendency to become VOC–limited, while the positive trends over Europe (0.3 decade^{-1}), US (0.63 decade^{-1}), and Africa (0.45 decade^{-1}), indicating a tendency to become more NOx–limited.

~~10.~~13. The estimated global mean tropospheric ozone radiative effect (TO3RE) is 1.21 [1.1 to 1.3] W m^{-2} which is increased by the doubling of NO$_X$ emissions (DoubNOx - CTL) by 0.36 [0.23 to 0.5] W m^{-2} and VOCs by -0.005 [-0.05 to 0.04] W m^{-2} (DoubVOC - CTL). However, halving NOx (HalfNOx - CTL) emissions shows a reduction in the global mean TO3RE by -0.12 [-0.2 to -0.05] W m^{-2} and VOC (HalfVOC - CTL) by -0.03 [-0.07 to 0.02] W m^{-2}.

~~11.~~14. We show that anthropogenic NO$_X$ emissions have a higher impact on tropospheric ozone levels, trends, and radiative effects than VOC emissions globally.

1119 Our study highlights the dominant role of anthropogenic NOx emissions in shaping tropospheric ozone
1120 trends, photochemical regimes, and radiative forcing over the past two decades. Sensitivity experiments
1121 reveal that NOx emission changes have a significantly larger impact on ozone levels and radiative
1122 forcing than VOCs, with regions transitioning from VOC-limited to NOx-limited regimes as NOx
1123 reductions continue. With current emission trends, air quality regulations, and industrial growth
1124 continuing to evolve, our study reinforces the need for region-specific mitigation strategies to
1125 effectively manage ozone pollution. This study emphasizes the importance of carefully balancing NOx
1126 and VOC controls to optimize air quality management and climate mitigation efforts. While climate
1127 change affects ozone chemistry, its impact over our study period (1998–2019) is minimal, given the
1128 relatively small global rate of temperature increase (~0.3–0.4°C) (IPCC AR6). Studies suggest that an
1129 ozone climate penalty emerges only after a 2–3°C temperature increase (Zanis et al., 2022), primarily
1130 in high-emission regions. Furthermore, rising temperatures increase water vapor, which reduces the
1131 ozone lifetime in remote areas. Thus, while climate change will play a growing role in future ozone
1132 variability, our findings confirm that anthropogenic emissions remain the dominant driver of recent
1133 ozone trends. As mitigation strategies evolve, targeted NOx and VOC controls must account for
1134 regional photochemical regimes, while future research should explore the potential interactions between
1135 climate change, natural VOCs, and ozone formation in a warming world.

1136 **Author's contribution**: SF and YE initiated the manuscript. SF made the model simulations.
1137 VS and SC did the analysis of model simulations. Satellite datasets are provided by JZ, BB,
1138 EF, IG, ID, MR, IS. All authors contributed to the writing of the manuscript.

1139

1140 **Competing interests:** At least one of the (co-)authors is a member of the editorial board of
1141 Atmospheric Chemistry and Physics.

1142

Acknowledgements

1144 S.F. acknowledge the high-performance computing at the Indian Institute of Tropical
1145 Meteorology Pune, India for supporting the model simulations. RJP was funded by the UK
1146 Natural Environment Research Council (NERC) by providing funding for the National Centre
1147 for Earth Observation (NCEO, award reference NE/R016518/1) and funding from the
1148 European Space Agency (ESA) Climate Change Initiative (CCI) post-doctoral fellowship
1149 scheme (award reference 4000137140).

Data availability

1151 Available from the TOAR FTP server (ftp://toar@ftpshare.al.noaa.gov).

Code availability

Available from the corresponding author upon reasonable request.

References:

Alvarado, L. M. A., Richter, A., Vrekoussis, M., Hilboll, A., Kalisz Hedegaard, A. B., Schneising, O., and Burrows, J. P.: Unexpected long-range transport of glyoxal and formaldehyde observed from the Copernicus Sentinel-5 Precursor satellite during the 2018 Canadian wildfires, Atmos. Chem. Phys., 20, 2057-2072, 10.5194/acp-20-2057-2020, 2020.

Anderson, D. C., Nicely, J. M., Wolfe, G. M., Hanisco, T. F., Salawitch, R. J., Canty, T. P., Dickerson, R. R., Apel, E. C., Baidar, S., Bannan, T. J., Blake, N. J., Chen, D., Dix, B., Fernandez, R. P., Hall, S. R., Hornbrook, R. S., Gregory Huey, L., Josse, B., Jöckel, P., Kinnison, D. E., Koenig, T. K., Le Breton, M., Marécal, V., Morgenstern, O., Oman, L. D., Pan, L. L., Percival, C., Plummer, D., Revell, L. E., Rozanov, E., Saiz-Lopez, A., Stenke, A., Sudo, K., Tilmes, S., Ullmann, K., Volkamer, R., Weinheimer, A. J., and Zeng, G.: Formaldehyde in the Tropical Western Pacific: Chemical Sources and Sinks, Convective Transport, and Representation in CAM-Chem and the CCMI Models, Journal of Geophysical Research: Atmospheres, 122, 11,201-211,226, https://doi.org/10.1002/2016JD026121, 2017.

Anglou, I., Glissenaar, I. A., Boersma, K. F., & Eskes, H. (2024). ESA CCI+ OMI L3 monthly mean NO2 columns [Data set]. Royal Netherlands Meteorological Institute (KNMI). https://doi.org/10.21944/cci-no2-omi-l3

Archibald, A. T., Neu, J. L., Elshorbany, Y. F., Cooper, O. R., Young, P. J., Akiyoshi, H., Cox, R. A., Coyle, M., Derwent, R. G., Deushi, M., Finco, A., Frost, G. J., Galbally, I. E., Gerosa, G., Granier, C., Griffiths, P. T., Hossaini, R., Hu, L., Jöckel, P., Josse, B., Lin, M. Y., Mertens, M., Morgenstern, O., Naja, M., Naik, V., Oltmans, S., Plummer, D. A., Revell, L. E., Saiz-Lopez, A., Saxena, P., Shin, Y. M., Shahid, I., Shallcross, D., Tilmes, S., Trickl, T., Wallington, T. J., Wang, T., Worden, H. M., and Zeng, G.: Tropospheric Ozone Assessment Report: A critical review of changes in the tropospheric ozone burden and budget from 1850 to 2100, Elementa: Science of the Anthropocene, 8, 10.1525/elementa.2020.034, 2020.

Barret, B., Gouzenes, Y., Le Flochmoen, E., and Ferrant, S.: Retrieval of Metop-A/IASI N2O Profiles and Validation with NDACC FTIR Data, Atmosphere, 12, 219, 2021.

Barret, B., Le Flochmoen, E., Sauvage, B., Pavelin, E., Matricardi, M., and Cammas, J. P.: The detection of post-monsoon tropospheric ozone variability over south Asia using IASI data, Atmos. Chem. Phys., 11, 9533-9548, 10.5194/acp-11-9533-2011, 2011.

Beig, G. and Singh, V.: Trends in tropical tropospheric column ozone from satellite data and MOZART model, Geophysical Research Letters, 34, https://doi.org/10.1029/2007GL030460, 2007.

Boersma, K. F., Vinken, G. C. M., and Eskes, H. J.: Representativeness errors in comparing chemistry transport and chemistry climate models with satellite UV–Vis tropospheric column retrievals, Geosci. Model Dev., 9, 875-898, 10.5194/gmd-9-875-2016, 2016.

Borbas, E. and Ruston, B.: The RTTOV UWiremis IR land surface emissivity module, Mission Report EUMETSAT NWPSAF-MO-VS-042. http://nwpsaf.eu/vs_reports/nwpsaf-mo-vs-042.pdf, 2010.

Chang, C.-Y., Faust, E., Hou, X., Lee, P., Kim, H. C., Hedquist, B. C., and Liao, K.-J.: Investigating ambient ozone formation regimes in neighboring cities of shale plays in the Northeast United States using photochemical modeling and satellite retrievals, Atmospheric Environment, 142, 152-170, https://doi.org/10.1016/j.atmosenv.2016.06.058, 2016.

Chang, K.-L., Cooper, O. R., Gaudel, A., Allaart, M., Ancellet, G., Clark, H., Godin-Beekmann, S., Leblanc, T., Van Malderen, R., Nédélec, P., Petropavlovskikh, I., Steinbrecht, W., Stübi, R., Tarasick, D. W., and Torres, C.: Impact of the COVID-19 Economic Downturn on Tropospheric Ozone Trends: An Uncertainty Weighted Data Synthesis for Quantifying Regional Anomalies Above Western North America and Europe, AGU Advances, 3, e2021AV000542, https://doi.org/10.1029/2021AV000542, 2022.

Chang, K.-L., Cooper, O. R., Rodriguez, G., Iraci, L. T., Yates, E. L., Johnson, M. S., Gaudel, A., Jaffe, D. A., Bernays, N., Clark, H., Effertz, P., Leblanc, T., Petropavlovskikh, I., Sauvage, B., and Tarasick, D. W.: Diverging Ozone Trends Above Western North America: Boundary Layer Decreases Versus Free Tropospheric Increases, Journal of Geophysical Research: Atmospheres, 128, e2022JD038090, https://doi.org/10.1029/2022JD038090, 2023.

Chen, Y., Wang, M., Yao, Y., Zeng, C., Zhang, W., Yan, H., Gao, P., Fan, L., and Ye, D.: Research on the ozone formation sensitivity indicator of four urban agglomerations of China using Ozone Monitoring Instrument (OMI) satellite data and ground-based measurements, Science of The Total Environment, 869, 161679, https://doi.org/10.1016/j.scitotenv.2023.161679, 2023.

Cohen, Y., Petetin, H., Thouret, V., Marécal, V., Josse, B., Clark, H., Sauvage, B., Fontaine, A., Athier, G., Blot, R., Boulanger, D., Cousin, J. M., and Nédélec, P.: Climatology and long-term evolution of ozone and carbon monoxide in the upper troposphere–lower stratosphere (UTLS) at northern midlatitudes, as seen by IAGOS from 1995 to 2013, Atmos. Chem. Phys., 18, 5415-5453, 10.5194/acp-18-5415-2018, 2018.

Cooper, O. R., Parrish, D. D., Ziemke, J., Balashov, N. V., Cupeiro, M., Galbally, I. E., Gilge, S., Horowitz, L., Jensen, N. R., Lamarque, J.-F., Naik, V., Oltmans, S. J., Schwab, J., Shindell, D. T., Thompson, A. M., Thouret, V., Wang, Y., and Zbinden, R. M.: Global distribution and trends of tropospheric ozone: An observation-based review, Elementa: Science of the Anthropocene, 2, 10.12952/journal.elementa.000029, 2014.

Cuesta, J., Kanaya, Y., Takigawa, M., Dufour, G., Eremenko, M., Foret, G., Miyazaki, K., and Beekmann, M.: Transboundary ozone pollution across East Asia: daily evolution and photochemical production analysed by IASI + GOME2 multispectral satellite observations and models, Atmos. Chem. Phys., 18, 9499-9525, 10.5194/acp-18-9499-2018, 2018.

Cuesta, J., Costantino, L., Beekmann, M., Siour, G., Menut, L., Bessagnet, B., Landi, T. C., Dufour, G., and Eremenko, M.: Ozone pollution during the COVID-19 lockdown in the spring of 2020 over Europe, analysed from satellite observations, in situ measurements, and models, Atmos. Chem. Phys., 22, 4471-4489, 10.5194/acp-22-4471-2022, 2022.

Cuesta, J., Eremenko, M., Liu, X., Dufour, G., Cai, Z., Höpfner, M., von Clarmann, T., Sellitto, P., Foret, G., Gaubert, B., Beekmann, M., Orphal, J., Chance, K., Spurr, R., and Flaud, J. M.:

Satellite observation of lowermost tropospheric ozone by multispectral synergism of IASI thermal infrared and GOME-2 ultraviolet measurements over Europe, Atmos. Chem. Phys., 13, 9675-9693, 10.5194/acp-13-9675-2013, 2013.

De Smedt, I., Stavrakou, T., Hendrick, F., Danckaert, T., Vlemmix, T., Pinardi, G., Theys, N., Lerot, C., Gielen, C., Vigouroux, C., Hermans, C., Fayt, C., Veefkind, P., Müller, J. F., and Van Roozendael, M.: Diurnal, seasonal and long-term variations of global formaldehyde columns inferred from combined OMI and GOME-2 observations, Atmos. Chem. Phys., 15, 12519-12545, 10.5194/acp-15-12519-2015, 2015.

De Smedt, I., Theys, N., Yu, H., Danckaert, T., Lerot, C., Compernolle, S., Van Roozendael, M., Richter, A., Hilboll, A., Peters, E., Pedergnana, M., Loyola, D., Beirle, S., Wagner, T., Eskes, H., van Geffen, J., Boersma, K. F., and Veefkind, P.: Algorithm theoretical baseline for formaldehyde retrievals from S5P TROPOMI and from the QA4ECV project, Atmos. Meas. Tech., 11, 2395-2426, 10.5194/amt-11-2395-2018, 2018.

De Smedt, I., Pinardi, G., Vigouroux, C., Compernolle, S., Bais, A., Benavent, N., Boersma, F., Chan, K. L., Donner, S., Eichmann, K. U., Hedelt, P., Hendrick, F., Irie, H., Kumar, V., Lambert, J. C., Langerock, B., Lerot, C., Liu, C., Loyola, D., Piters, A., Richter, A., Rivera Cárdenas, C., Romahn, F., Ryan, R. G., Sinha, V., Theys, N., Vlietinck, J., Wagner, T., Wang, T., Yu, H., and Van Roozendael, M.: Comparative assessment of TROPOMI and OMI formaldehyde observations and validation against MAX-DOAS network column measurements, Atmos. Chem. Phys., 21, 12561-12593, 10.5194/acp-21-12561-2021, 2021.

Duncan, B. N., Yoshida, Y., Olson, J. R., Sillman, S., Martin, R. V., Lamsal, L., Hu, Y., Pickering, K. E., Retscher, C., Allen, D. J., and Crawford, J. H.: Application of OMI observations to a space-based indicator of NOx and VOC controls on surface ozone formation, Atmospheric Environment, 44, 2213-2223, https://doi.org/10.1016/j.atmosenv.2010.03.010, 2010.

Edwards, J. M. and Slingo, A.: Studies with a flexible new radiation code. I: Choosing a configuration for a large-scale model, Quarterly Journal of the Royal Meteorological Society, 122, 689-719, https://doi.org/10.1002/qj.49712253107, 1996.

Edwards, D. P., Martínez-Alonso, S., Jo, D. S., Ortega, I., Emmons, L. K., Orlando, J. J., Worden, H. M., Kim, J., Lee, H., Park, J., and Hong, H.: Quantifying the diurnal variation in atmospheric NO2 from Geostationary Environment Monitoring Spectrometer (GEMS) observations, Atmos. Chem. Phys., 24, 8943–8961, https://doi.org/10.5194/acp-24-8943-2024, 2024.

Elshorbany, Y., Ziemke, J., Strode, S., Petetin, H., Miyazaki, K., De Smedt, I., Pickering, K., Seguel, R., Worden, H., Emmerichs, T., Taraborrelli, D., Cazorla, M., Fadnavis, S., Buchholz, R., Gaubert, B., Rojas, N., Nogueira, T., Salameh, T., and Huang, M.: Tropospheric Ozone Precursors: Global and Regional Distributions, Trends and Variability, EGUsphere, 2024, 1-57, 10.5194/egusphere-2024-720, 2024.

Emmons, L. K., Apel, E. C., Lamarque, J. F., Hess, P. G., Avery, M., Blake, D., Brune, W., Campos, T., Crawford, J., DeCarlo, P. F., Hall, S., Heikes, B., Holloway, J., Jimenez, J. L., Knapp, D. J., Kok, G., Mena-Carrasco, M., Olson, J., O'Sullivan, D., Sachse, G., Walega, J., Weibring, P., Weinheimer, A., and Wiedinmyer, C.: Impact of Mexico City emissions on regional air quality from MOZART-4 simulations, Atmos. Chem. Phys., 10, 6195-6212, 10.5194/acp-10-6195-2010, 2010.

EPA, O. U. Air Pollutant Emissions Trends Data. https://www.epa.gov/air-emissions-inventories/air-pollutant-emissions-trends-data, 2023

Fadnavis, S., Sabin, T. P., Rap, A., Müller, R., Kubin, A., and Heinold, B.: The impact of COVID-19 lockdown measures on the Indian summer monsoon, Environmental Research Letters, 16, 074054, 10.1088/1748-9326/ac109c, 2021a.

Fadnavis, S., Heinold, B., Sabin, T. P., Kubin, A., Huang, K., Rap, A., and Müller, R.: Air pollution reductions caused by the COVID-19 lockdown open up a way to preserve the Himalayan glaciers, Atmos. Chem. Phys., 23, 10439-10449, 10.5194/acp-23-10439-2023, 2023.

Fadnavis, S., Sabin, T. P., Roy, C., Rowlinson, M., Rap, A., Vernier, J.-P., and Sioris, C. E.: Elevated aerosol layer over South Asia worsens the Indian droughts, Scientific Reports, 9, 10268, 10.1038/s41598-019-46704-9, 2019a.

Fadnavis, S., Müller, R., Kalita, G., Rowlinson, M., Rap, A., Li, J. L. F., Gasparini, B., and Laakso, A.: The impact of recent changes in Asian anthropogenic emissions of SO2 on sulfate loading in the upper troposphere and lower stratosphere and the associated radiative changes, Atmos. Chem. Phys., 19, 9989-10008, 10.5194/acp-19-9989-2019, 2019b.

Fadnavis, S., Chavan, P., Joshi, A., Sonbawne, S. M., Acharya, A., Devara, P. C. S., Rap, A., Ploeger, F., and Müller, R.: Tropospheric warming over the northern Indian Ocean caused by South Asian anthropogenic aerosols: possible impact on the upper troposphere and lower stratosphere, Atmos. Chem. Phys., 22, 7179-7191, 10.5194/acp-22-7179-2022, 2022.

Fadnavis, S., Müller, R., Chakraborty, T., Sabin, T. P., Laakso, A., Rap, A., Griessbach, S., Vernier, J.-P., and Tilmes, S.: The role of tropical volcanic eruptions in exacerbating Indian droughts, Scientific Reports, 11, 2714, 10.1038/s41598-021-81566-0, 2021b.

Fiore, A. M., Hancock, S. E., Lamarque, J.-F., Correa, G. P., Chang, K.-L., Ru, M., Cooper, O., Gaudel, A., Polvani, L. M., Sauvage, B., and Ziemke, J. R.: Understanding recent tropospheric ozone trends in the context of large internal variability: a new perspective from chemistry-climate model ensembles, Environmental Research: Climate, 1, 025008, 10.1088/2752-5295/ac9cc2, 2022.

Fleming, Z. L., Doherty, R. M., von Schneidemesser, E., Malley, C. S., Cooper, O. R., Pinto, J. P., Colette, A., Xu, X., Simpson, D., Schultz, M. G., Lefohn, A. S., Hamad, S., Moolla, R., Solberg, S., and Feng, Z.: Tropospheric Ozone Assessment Report: Present-day ozone distribution and trends relevant to human health, Elementa: Science of the Anthropocene, 6, 10.1525/elementa.273, 2018.

Forster, P., Storelvmo, T., Armour, K., Collins, W., Dufresne, J.-L., Frame, D., Lunt, D. J., Mauritsen, T., Palmer, M. D., Watanabe, M., Wild, M., and Zhang, H.: The Earth's Energy Budget, Climate Feedbacks and Climate Sensitivity, in: Climate Change 2021: The Physical Science Basis. Contribution of Working Group I to the Sixth Assessment Report of the Intergovernmental Panel on Climate Change [Masson-Delmotte, V., P. Zhai, A. Pirani, S.L. Connors, C. Péan, S. Berger, N. Caud, Y. Chen, L. Goldfarb, M.I. Gomis, M. Huang, K. Leitzell, E. Lonnoy, J.B.R. Matthews, T.K. Maycock, T. Waterfield, O. Yelekçi, R. Yu, and B. Zhou (eds.)], edited by: Intergovernmental Panel on Climate, C., Cambridge University Press, Cambridge, 923-1054, DOI: 10.1017/9781009157896.009, 2021.

Forster, P. M., Smith, C., Walsh, T., Lamb, W. F., Lamboll, R., Hall, B., Hauser, M., Ribes, A., Rosen, D., Gillett, N. P., Palmer, M. D., Rogelj, J., von Schuckmann, K., Trewin, B., Allen, M., Andrew, R., Betts, R. A., Borger, A., Boyer, T., Broersma, J. A., Buontempo, C., Burgess, S., Cagnazzo, C., Cheng, L., Friedlingstein, P., Gettelman, A., Gütschow, J., Ishii, M., Jenkins, S., Lan, X., Morice, C., Mühle, J., Kadow, C., Kennedy, J., Killick, R. E., Krummel, P. B., Minx, J. C., Myhre, G., Naik, V., Peters, G. P., Pirani, A., Pongratz, J., Schleussner, C. F., Seneviratne, S. I., Szopa, S., Thorne, P., Kovilakam, M. V. M., Majamäki, E., Jalkanen, J. P., van Marle, M., Hoesly, R. M., Rohde, R., Schumacher, D., van der Werf, G., Vose, R., Zickfeld, K., Zhang, X., Masson-Delmotte, V., and Zhai, P.: Indicators of Global Climate Change 2023: annual update of key indicators of the state of the climate system and human influence, Earth Syst. Sci. Data, 16, 2625-2658, 10.5194/essd-16-2625-2024, 2024.

Gaudel, A., Bourgeois, I., Li, M., Chang, K. L., Ziemke, J., Sauvage, B., Stauffer, R. M., Thompson, A. M., Kollonige, D. E., Smith, N., Hubert, D., Keppens, A., Cuesta, J., Heue, K. P., Veefkind, P., Aikin, K., Peischl, J., Thompson, C. R., Ryerson, T. B., Frost, G. J., McDonald, B. C., and Cooper, O. R.: Tropical tropospheric ozone distribution and trends from in situ and satellite data, EGUsphere, 2024, 1-51, 10.5194/egusphere-2023-3095, 2024.

Gaudel, A., Cooper, O. R., Ancellet, G., Barret, B., Boynard, A., Burrows, J. P., Clerbaux, C., Coheur, P.-F., Cuesta, J., Cuevas, E., Doniki, S., Dufour, G., Ebojie, F., Foret, G., Garcia, O., Granados-Muñoz, M. J., Hannigan, J. W., Hase, F., Hassler, B., Huang, G., Hurtmans, D., Jaffe, D., Jones, N., Kalabokas, P., Kerridge, B., Kulawik, S., Latter, B., Leblanc, T., Le Flochmoën, E., Lin, W., Liu, J., Liu, X., Mahieu, E., McClure-Begley, A., Neu, J. L., Osman, M., Palm, M., Petetin, H., Petropavlovskikh, I., Querel, R., Rahpoe, N., Rozanov, A., Schultz, M. G., Schwab, J., Siddans, R., Smale, D., Steinbacher, M., Tanimoto, H., Tarasick, D. W., Thouret, V., Thompson, A. M., Trickl, T., Weatherhead, E., Wespes, C., Worden, H. M., Vigouroux, C., Xu, X., Zeng, G., and Ziemke, J.: Tropospheric Ozone Assessment Report: Present-day distribution and trends of tropospheric ozone relevant to climate and global atmospheric chemistry model evaluation, Elementa: Science of the Anthropocene, 6, 10.1525/elementa.291, 2018.

Glissenaar, I. A., Anglou, I., Boersma, K. F., & Eskes. H, ESA CCI+ TROPOMI L3 monthly mean NO2 columns [Data set]. Royal Netherlands Meteorological Institute (KNMI). https://doi.org/10.21944/CCI-NO2-TROPOMI-L3, 2024

Goldberg, D. L., Anenberg, S. C., Kerr, G. H., Mohegh, A., Lu, Z., and Streets, D. G.: TROPOMI NO2 in the United States: A Detailed Look at the Annual Averages, Weekly Cycles, Effects of Temperature, and Correlation With Surface NO2 Concentrations, Earth's Future, 9, e2020EF001665, https://doi.org/10.1029/2020EF001665, 2021.

Griffiths, P. T., Murray, L. T., Zeng, G., Shin, Y. M., Abraham, N. L., Archibald, A. T., Deushi, M., Emmons, L. K., Galbally, I. E., Hassler, B., Horowitz, L. W., Keeble, J., Liu, J., Moeini, O., Naik, V., O'Connor, F. M., Oshima, N., Tarasick, D., Tilmes, S., Turnock, S. T., Wild, O., Young, P. J., and Zanis, P.: Tropospheric ozone in CMIP6 simulations, Atmos. Chem. Phys., 21, 4187-4218, 10.5194/acp-21-4187-2021, 2021.

Guan, J., Jin, B., Ding, Y., Wang, W., Li, G., and Ciren, P.: Global Surface HCHO Distribution Derived from Satellite Observations with Neural Networks Technique, Remote Sensing, 13, 4055, 2021.

Guenther, A. B., Jiang, X., Heald, C. L., Sakulyanontvittaya, T., Duhl, T., Emmons, L. K., and Wang, X.: The Model of Emissions of Gases and Aerosols from Nature version 2.1 (MEGAN2.1): an extended and updated framework for modeling biogenic emissions, Geosci. Model Dev., 5, 1471-1492, 10.5194/gmd-5-1471-2012, 2012.

Gulev, S. K., Thorne, P. W., Ahn, J., Dentener, F. J., Domingues, C. M., Gerland, S., Gong, D., Kaufman, D. S., Nnamchi, H. C., Quaas, J., Rivera, J. A., Sathyendranath, S., Smith, S. L., Trewin, B., von Schuckmann, K., and Vose, R. S.: Changing State of the Climate System, in: Climate Change 2021 – The Physical Science Basis: Working Group I Contribution to the Sixth Assessment Report of the Intergovernmental Panel on Climate Change [Masson-Delmotte, V., P. Zhai, A. Pirani, S.L. Connors, C. Péan, S. Berger, N. Caud, Y. Chen, L. Goldfarb, M.I. Gomis, M. Huang, K. Leitzell, E. Lonnoy, J.B.R. Matthews, T.K. Maycock, T. Waterfield, O. Yelekçi, R. Yu, and B. Zhou (eds.)], edited by: Intergovernmental Panel on Climate, C., Cambridge University Press, Cambridge, 287-422, DOI: 10.1017/9781009157896.004, 2021.

Henrot, A. J., Stanelle, T., Schröder, S., Siegenthaler, C., Taraborrelli, D., and Schultz, M. G.: Implementation of the MEGAN (v2.1) biogenic emission model in the ECHAM6-HAMMOZ chemistry climate model, Geosci. Model Dev., 10, 903-926, 10.5194/gmd-10-903-2017, 2017.

Hoffmann, L. and Spang, R.: An assessment of tropopause characteristics of the ERA5 and ERA-Interim meteorological reanalyses, Atmos. Chem. Phys., 22, 4019–4046, https://doi.org/10.5194/acp-22-4019-2022, 2022.

Jin, X. and Holloway, T.: Spatial and temporal variability of ozone sensitivity over China observed from the Ozone Monitoring Instrument, Journal of Geophysical Research: Atmospheres, 120, 7229-7246, https://doi.org/10.1002/2015JD023250, 2015.

Jin, X., Fiore, A., Boersma, K. F., Smedt, I. D., and Valin, L.: Inferring Changes in Summertime Surface Ozone–NOx–VOC Chemistry over U.S. Urban Areas from Two Decades of Satellite and Ground-Based Observations, Environmental Science & Technology, 54, 6518-6529, 10.1021/acs.est.9b07785, 2020.

Jin, X., Fiore, A. M., Murray, L. T., Valin, L. C., Lamsal, L. N., Duncan, B., Folkert Boersma, K., De Smedt, I., Abad, G. G., Chance, K., and Tonnesen, G. S.: Evaluating a Space-Based Indicator of Surface Ozone-NO-VOC Sensitivity Over Midlatitude Source Regions and Application to Decadal Trends, Journal of Geophysical Research: Atmospheres, 122, 10,439-410,461, https://doi.org/10.1002/2017JD026720, 2017.

Johnson, M. S., Philip, S., Meech, S., Kumar, R., Sorek-Hamer, M., Shiga, Y. P., and Jung, J.: Insights into the long-term (2005–2021) spatiotemporal evolution of summer ozone production sensitivity in the Northern Hemisphere derived with the Ozone Monitoring Instrument (OMI), Atmos. Chem. Phys., 24, 10363-10384, 10.5194/acp-24-10363-2024, 2024.

Kinnison, D. E., Brasseur, G. P., Walters, S., Garcia, R. R., Marsh, D. R., Sassi, F., Harvey, V. L., Randall, C. E., Emmons, L., Lamarque, J. F., Hess, P., Orlando, J. J., Tie, X. X., Randel, W., Pan, L. L., Gettelman, A., Granier, C., Diehl, T., Niemeier, U., and Simmons, A. J.: Sensitivity of chemical tracers to meteorological parameters in the MOZART-3 chemical transport model, Journal of Geophysical Research: Atmospheres, 112, https://doi.org/10.1029/2006JD007879, 2007.

Kleinman, L. I.: Low and high NOx tropospheric photochemistry, Journal of Geophysical Research: Atmospheres, 99, 16831-16838, https://doi.org/10.1029/94JD01028, 1994.

Kumar, V., Beirle, S., Dörner, S., Mishra, A. K., Donner, S., Wang, Y., Sinha, V., and Wagner, T.: Long-term MAX-DOAS measurements of NO2, HCHO, and aerosols and evaluation of corresponding satellite data products over Mohali in the Indo-Gangetic Plain, Atmos. Chem. Phys., 20, 14183-14235, 10.5194/acp-20-14183-2020, 2020.

Lamarque, J. F., Emmons, L. K., Hess, P. G., Kinnison, D. E., Tilmes, S., Vitt, F., Heald, C. L., Holland, E. A., Lauritzen, P. H., Neu, J., Orlando, J. J., Rasch, P. J., and Tyndall, G. K.: CAM-chem: description and evaluation of interactive atmospheric chemistry in the Community Earth System Model, Geosci. Model Dev., 5, 369-411, 10.5194/gmd-5-369-2012, 2012.

Lamarque, J. F., Bond, T. C., Eyring, V., Granier, C., Heil, A., Klimont, Z., Lee, D., Liousse, C., Mieville, A., Owen, B., Schultz, M. G., Shindell, D., Smith, S. J., Stehfest, E., Van Aardenne, J., Cooper, O. R., Kainuma, M., Mahowald, N., McConnell, J. R., Naik, V., Riahi, K., and van Vuuren, D. P.: Historical (1850–2000) gridded anthropogenic and biomass burning emissions of reactive gases and aerosols: methodology and application, Atmos. Chem. Phys., 10, 7017-7039, 10.5194/acp-10-7017-2010, 2010.

Lamsal, L. N., Krotkov, N. A., Vasilkov, A., Marchenko, S., Qin, W., Yang, E. S., Fasnacht, Z., Joiner, J., Choi, S., Haffner, D., Swartz, W. H., Fisher, B., and Bucsela, E.: Ozone Monitoring Instrument (OMI) Aura nitrogen dioxide standard product version 4.0 with improved surface and cloud treatments, Atmos. Meas. Tech., 14, 455-479, 10.5194/amt-14-455-2021, 2021.

Lee, H. J., Chang, L. S., Jaffe, D. A., Bak, J., Liu, X., Abad, G. G., Jo, H. Y., Jo, Y. J., Lee, J. B., Yang, G. H., Kim, J. M., and Kim, C. H.: Satellite Based Diagnosis and Numerical Verification of Ozone Formation Regimes over Nine Megacities in East Asia, Remote Sensing, 14, 1285, 2022.

Lefohn, A. S., Malley, C. S., Simon, H., Wells, B., Xu, X., Zhang, L., and Wang, T.: Responses of human health and vegetation exposure metrics to changes in ozone concentration distributions in the European Union, United States, and China, Atmospheric Environment, 152, 123-145, https://doi.org/10.1016/j.atmosenv.2016.12.025, 2017.

Li, M., Kurokawa, J., Zhang, Q., Woo, J. H., Morikawa, T., Chatani, S., Lu, Z., Song, Y., Geng, G., Hu, H., Kim, J., Cooper, O. R., and McDonald, B. C.: MIXv2: a long-term mosaic emission inventory for Asia (2010–2017), Atmos. Chem. Phys., 24, 3925-3952, 10.5194/acp-24-3925-2024, 2024.

Li, S., Yang, Y., Wang, H., Li, P., Li, K., Ren, L., Wang, P., Li, B., Mao, Y., and Liao, H.: Rapid increase in tropospheric ozone over Southeast Asia attributed to changes in precursor emission source regions and sectors, Atmospheric Environment, 304, 119776, https://doi.org/10.1016/j.atmosenv.2023.119776, 2023.

Lin, M., Horowitz, L. W., Oltmans, S. J., Fiore, A. M., and Fan, S.: Tropospheric ozone trends at Mauna Loa Observatory tied to decadal climate variability, Nature Geoscience, 7, 136-143, 10.1038/ngeo2066, 2014.

Liu, J., Strode, S. A., Liang, Q., Oman, L. D., Colarco, P. R., Fleming, E. L., Manyin, M. E., Douglass, A. R., Ziemke, J. R., Lamsal, L. N., and Li, C.: Change in Tropospheric Ozone in the Recent Decades and Its Contribution to Global Total Ozone, Journal of Geophysical Research: Atmospheres, 127, e2022JD037170, https://doi.org/10.1029/2022JD037170, 2022.

Lu, X., Zhang, L., Liu, X., Gao, M., Zhao, Y., and Shao, J.: Lower tropospheric ozone over India and its linkage to the South Asian monsoon, Atmos. Chem. Phys., 18, 3101-3118, 10.5194/acp-18-3101-2018, 2018.

Mahajan, A. S., De Smedt, I., Biswas, M. S., Ghude, S., Fadnavis, S., Roy, C., and van Roozendael, M.: Inter-annual variations in satellite observations of nitrogen dioxide and formaldehyde over India, Atmospheric Environment, 116, 194-201, https://doi.org/10.1016/j.atmosenv.2015.06.004, 2015.

Martin, R. V., Fiore, A. M., and Van Donkelaar, A.: Space-based diagnosis of surface ozone sensitivity to anthropogenic emissions, Geophysical Research Letters, 31, https://doi.org/10.1029/2004GL019416, 2004.

Matricardi, M., Chevallier, F., Kelly, G., and Thépaut, J.-N.: An improved general fast radiative transfer model for the assimilation of radiance observations, Quarterly Journal of the Royal Meteorological Society, 130, 153-173, https://doi.org/10.1256/qj.02.181, 2004.

Millet, D. B., Jacob, D. J., Boersma, K. F., Fu, T. M., Kurosu, T. P., Chance, K., Heald, C. L., and Guenther, A.: Spatial distribution of isoprene emissions from North America derived from formaldehyde column measurements by the OMI satellite sensor, Journal of Geophysical Research: Atmospheres, 113, https://doi.org/10.1029/2007JD008950, 2008.

Mills, G., Pleijel, H., Malley, C. S., Sinha, B., Cooper, O. R., Schultz, M. G., Neufeld, H. S., Simpson, D., Sharps, K., Feng, Z., Gerosa, G., Harmens, H., Kobayashi, K., Saxena, P., Paoletti, E., Sinha, V., and Xu, X.: Tropospheric Ozone Assessment Report: Present-day tropospheric ozone distribution and trends relevant to vegetation, Elementa: Science of the Anthropocene, 6, 10.1525/elementa.302, 2018.

Monks, P. S., Archibald, A. T., Colette, A., Cooper, O., Coyle, M., Derwent, R., Fowler, D., Granier, C., Law, K. S., Mills, G. E., Stevenson, D. S., Tarasova, O., Thouret, V., von Schneidemesser, E., Sommariva, R., Wild, O., and Williams, M. L.: Tropospheric ozone and its precursors from the urban to the global scale from air quality to short-lived climate forcer, Atmos. Chem. Phys., 15, 8889-8973, 10.5194/acp-15-8889-2015, 2015.

O3 (IASI+GOME2) – IASI portal: https://iasi.aeris-data.fr/o3_iago2/, last access: 28 May 2024

Okamoto, S., Cuesta, J., Beekmann, M., Dufour, G., Eremenko, M., Miyazaki, K., Boonne, C., Tanimoto, H., and Akimoto, H.: Impact of different sources of precursors on an ozone pollution outbreak over Europe analysed with IASI+GOME2 multispectral satellite observations and model simulations, Atmos. Chem. Phys., 23, 7399-7423, 10.5194/acp-23-7399-2023, 2023.

Pope, R. J., Rap, A., Pimlott, M. A., Barret, B., Le Flochmoen, E., Kerridge, B. J., Siddans, R., Latter, B. G., Ventress, L. J., Boynard, A., Retscher, C., Feng, W., Rigby, R., Dhomse, S. S., Wespes, C., and Chipperfield, M. P.: Quantifying the tropospheric ozone radiative effect and its temporal evolution in the satellite era, Atmos. Chem. Phys., 24, 3613-3626, 10.5194/acp-24-3613-2024, 2024.

Prather, M., and Zhu X., Lifetimes and timescales of tropospheric ozone, Lifetimes and timescales of tropospheric ozone. Elem, 12, 1, 2024, doi:10.1525/elementa.2023.00112.

Putero, D., Cristofanelli, P., Chang, K. L., Dufour, G., Beachley, G., Couret, C., Effertz, P., Jaffe, D. A., Kubistin, D., Lynch, J., Petropavlovskikh, I., Puchalski, M., Sharac, T., Sive, B. C., Steinbacher, M., Torres, C., and Cooper, O. R.: Fingerprints of the COVID-19 economic downturn and recovery on ozone anomalies at high-elevation sites in North America and western Europe, Atmos. Chem. Phys., 23, 15693-15709, 10.5194/acp-23-15693-2023, 2023.

Rap, A., Richards, N. A. D., Forster, P. M., Monks, S. A., Arnold, S. R., and Chipperfield, M. P.: Satellite constraint on the tropospheric ozone radiative effect, Geophysical Research Letters, 42, 5074-5081, https://doi.org/10.1002/2015GL064037, 2015.

Rast, S., Schultz, M. G., Bey, I., van Noije, T., Aghedo, A. M., Brasseur, G. P., Diehl, T., Esch, M., Ganzeveld, L., Kirchner, I., Kornblueh, L., Rhodin, A., Roeckner, E., Schmidt, H., Schroder, S., Schulzweida, U., Stier, P., Thomas, K., and Walters, S.: Evaluation of the tropospheric chemistry general circulation model ECHAM5–MOZ and its application to the analysis of the chemical composition of the troposphere with an emphasis on the late RETRO period 1990–2000, Max-Planck-Institut für Meteorologie, Hamburg114, 2014.

Reick, C. H., Raddatz, T., Brovkin, V., and Gayler, V.: Representation of natural and anthropogenic land cover change in MPI-ESM, Journal of Advances in Modeling Earth Systems, 5, 459-482, https://doi.org/10.1002/jame.20022, 2013.

Ren, J., Guo, F., and Xie, S.: Diagnosing ozone–NOx–VOC sensitivity and revealing causes of ozone increases in China based on 2013–2021 satellite retrievals, Atmos. Chem. Phys., 22, 15035-15047, 10.5194/acp-22-15035-2022, 2022.

Riese, M. and Ploeger, F. and Rap, A. and Vogel, B. and Konopka, P. and Dameris, M. and Forster, P.: Impact of uncertainties in atmospheric mixing on simulated UTLS composition and related radiative effects, J. Geophys. Res., 117, D16305, 10.1029/2012JD017751, 2012

Roberts, S. J., Salawitch, R. J., Wolfe, G. M., Marvin, M. R., Canty, T. P., Allen, D. J., Hall-Quinlan, D. L., Krask, D. J., and Dickerson, R. R.: Multidecadal trends in ozone chemistry in the Baltimore Washington Region, Atmospheric Environment, 285, 119239, https://doi.org/10.1016/j.atmosenv.2022.119239, 2022.

Rosanka, S., Franco, B., Clarisse, L., Coheur, P. F., Pozzer, A., Wahner, A., and Taraborrelli, D.: The impact of organic pollutants from Indonesian peatland fires on the tropospheric and lower stratospheric composition, Atmos. Chem. Phys., 21, 11257-11288, 10.5194/acp-21-11257-2021, 2021.

Rothman, L. S., Jacquemart, D., Barbe, A., Chris Benner, D., Birk, M., Brown, L. R., Carleer, M. R., Chackerian, C., Chance, K., Coudert, L. H., Dana, V., Devi, V. M., Flaud, J. M., Gamache, R. R., Goldman, A., Hartmann, J. M., Jucks, K. W., Maki, A. G., Mandin, J. Y., Massie, S. T., Orphal, J., Perrin, A., Rinsland, C. P., Smith, M. A. H., Tennyson, J., Tolchenov, R. N., Toth, R. A., Vander Auwera, J., Varanasi, P., and Wagner, G.: The HITRAN 2004 molecular spectroscopic database, Journal of Quantitative Spectroscopy and Radiative Transfer, 96, 139-204, https://doi.org/10.1016/j.jqsrt.2004.10.008, 2005.

Rowlinson, M. J., Rap, A., Hamilton, D. S., Pope, R. J., Hantson, S., Arnold, S. R., Kaplan, J. O., Arneth, A., Chipperfield, M. P., Forster, P. M., and Nieradzik, L.: Tropospheric ozone radiative forcing uncertainty due to pre-industrial fire and biogenic emissions, Atmos. Chem. Phys., 20, 10937-10951, 10.5194/acp-20-10937-2020, 2020.

Saunders, R., Matricardi, M., and Brunel, P.: An improved fast radiative transfer model for assimilation of satellite radiance observations, Quarterly Journal of the Royal Meteorological Society, 125, 1407-1425, https://doi.org/10.1002/qj.1999.49712555615, 1999.

Schroeder, J. R., Crawford, J. H., Fried, A., Walega, J., Weinheimer, A., Wisthaler, A., Müller, M., Mikoviny, T., Chen, G., Shook, M., Blake, D. R., and Tonnesen, G. S.: New insights into the column CH2O/NO2 ratio as an indicator of near-surface ozone sensitivity, Journal of Geophysical Research: Atmospheres, 122, 8885-8907, https://doi.org/10.1002/2017JD026781, 2017.

Schultz, M. G., Stadtler, S., Schröder, S., Taraborrelli, D., Franco, B., Krefting, J., Henrot, A., Ferrachat, S., Lohmann, U., Neubauer, D., Siegenthaler-Le Drian, C., Wahl, S., Kokkola, H., Kühn, T., Rast, S., Schmidt, H., Stier, P., Kinnison, D., Tyndall, G. S., Orlando, J. J., and Wespes, C.: The chemistry–climate model ECHAM6.3-HAM2.3-MOZ1.0, Geosci. Model Dev., 11, 1695-1723, 10.5194/gmd-11-1695-2018, 2018.

Schultz, M. G., Schröder, S., Lyapina, O., Cooper, O. R., Galbally, I., Petropavlovskikh, I., von Schneidemesser, E., Tanimoto, H., Elshorbany, Y., Naja, M., Seguel, R. J., Dauert, U., Eckhardt, P., Feigenspan, S., Fiebig, M., Hjellbrekke, A.-G., Hong, Y.-D., Kjeld, P. C., Koide, H., Lear, G., Tarasick, D., Ueno, M., Wallasch, M., Baumgardner, D., Chuang, M.-T., Gillett, R., Lee, M., Molloy, S., Moolla, R., Wang, T., Sharps, K., Adame, J. A., Ancellet, G., Apadula, F., Artaxo, P., Barlasina, M. E., Bogucka, M., Bonasoni, P., Chang, L., Colomb, A., Cuevas-Agulló, E., Cupeiro, M., Degorska, A., Ding, A., Fröhlich, M., Frolova, M., Gadhavi, H., Gheusi, F., Gilge, S., Gonzalez, M. Y., Gros, V., Hamad, S. H., Helmig, D., Henriques, D., Hermansen, O., Holla, R., Hueber, J., Im, U., Jaffe, D. A., Komala, N., Kubistin, D., Lam, K.-S., Laurila, T., Lee, H., Levy, I., Mazzoleni, C., Mazzoleni, L. R., McClure-Begley, A., Mohamad, M., Murovec, M., Navarro-Comas, M., Nicodim, F., Parrish, D., Read, K. A., Reid, N., Ries, L., Saxena, P., Schwab, J. J., Scorgie, Y., Senik, I., Simmonds, P., Sinha, V., Skorokhod, A. I., Spain, G., Spangl, W., Spoor, R., Springston, S. R., Steer, K., Steinbacher, M., Suharguniyawan, E., Torre, P., Trickl, T., Weili, L., Weller, R., Xiaobin, X., Xue, L., and Zhiqiang, M.: Tropospheric Ozone Assessment Report: Database and metrics data of global surface ozone observations, Elementa: Science of the Anthropocene, 5, 10.1525/elementa.244, 2017.

Scott, C. E., Monks, S. A., Spracklen, D. V., Arnold, S. R., Forster, P. M., Rap, A., Äijälä, M., Artaxo, P., Carslaw, K. S., Chipperfield, M. P., Ehn, M., Gilardoni, S., Heikkinen, L., Kulmala, M., Petäjä, T., Reddington, C. L. S., Rizzo, L. V., Swietlicki, E., Vignati, E., and Wilson, C.: Impact on short-lived climate forcers increases projected warming due to deforestation, Nature Communications, 9, 157, 10.1038/s41467-017-02412-4, 2018.

Shen, L., Jacob, D. J., Zhu, L., Zhang, Q., Zheng, B., Sulprizio, M. P., Li, K., De Smedt, I., González Abad, G., Cao, H., Fu, T.-M., and Liao, H.: The 2005–2016 Trends of Formaldehyde Columns Over China Observed by Satellites: Increasing Anthropogenic Emissions of Volatile Organic Compounds and Decreasing Agricultural Fire Emissions, Geophysical Research Letters, 46, 4468-4475, https://doi.org/10.1029/2019GL082172, 2019.

Sillman, S.: The use of NO , H2O2, and HNO3 as indicators for ozone-NO -hydrocarbon sensitivity in urban locations, Journal of Geophysical Research: Atmospheres, 100, 14175-14188, https://doi.org/10.1029/94JD02953, 1995.

Sillman, S., Logan, J. A., and Wofsy, S. C.: The sensitivity of ozone to nitrogen oxides and hydrocarbons in regional ozone episodes, Journal of Geophysical Research: Atmospheres, 95, 1837-1851, https://doi.org/10.1029/JD095iD02p01837, 1990.

Sofieva, V. F., Tamminen, J., Kyrölä, E., Mielonen, T., Veefkind, P., Hassler, B., and Bodeker, G. E.: A novel tropopause-related climatology of ozone profiles, Atmos. Chem. Phys., 14, 283-299, 10.5194/acp-14-283-2014, 2014.

Souri, A. H., Choi, Y., Jeon, W., Woo, J.-H., Zhang, Q., and Kurokawa, J.-i.: Remote sensing evidence of decadal changes in major tropospheric ozone precursors over East Asia, Journal of Geophysical Research - Atmospheres, 122, 2474-2492, https://doi.org/10.1002/2016JD025663, 2017.

Stadtler, S., Simpson, D., Schröder, S., Taraborrelli, D., Bott, A., and Schultz, M.: Ozone impacts of gas–aerosol uptake in global chemistry transport models, Atmos. Chem. Phys., 18, 3147-3171, 10.5194/acp-18-3147-2018, 2018.

Steinbrecht, W., Kubistin, D., Plass-Dülmer, C., Davies, J., Tarasick, D. W., von der Gathen, P., Deckelmann, H., Jepsen, N., Kivi, R., Lyall, N., Palm, M., Notholt, J., Kois, B., Oelsner, P., Allaart, M., Piters, A., Gill, M., Van Malderen, R., Delcloo, A. W., Sussmann, R., Mahieu, E., Servais, C., Romanens, G., Stübi, R., Ancellet, G., Godin-Beekmann, S., Yamanouchi, S., Strong, K., Johnson, B., Cullis, P., Petropavlovskikh, I., Hannigan, J. W., Hernandez, J.-L., Diaz Rodriguez, A., Nakano, T., Chouza, F., Leblanc, T., Torres, C., Garcia, O., Röhling, A. N., Schneider, M., Blumenstock, T., Tully, M., Paton-Walsh, C., Jones, N., Querel, R., Strahan, S., Stauffer, R. M., Thompson, A. M., Inness, A., Engelen, R., Chang, K.-L., and Cooper, O. R.: COVID-19 Crisis Reduces Free Tropospheric Ozone Across the Northern Hemisphere, Geophysical Research Letters, 48, e2020GL091987, https://doi.org/10.1029/2020GL091987, 2021.

Stevens, B., Giorgetta, M., Esch, M., Mauritsen, T., Crueger, T., Rast, S., Salzmann, M., Schmidt, H., Bader, J., Block, K., Brokopf, R., Fast, I., Kinne, S., Kornblueh, L., Lohmann, U., Pincus, R., Reichler, T., and Roeckner, E.: Atmospheric component of the MPI-M Earth System Model: ECHAM6, Journal of Advances in Modeling Earth Systems , 5, 146-172, 10.1002/jame.20015, 2013.

Stevenson, D. S., Dentener, F. J., Schultz, M. G., Ellingsen, K., van Noije, T. P. C., Wild, O., Zeng, G., Amann, M., Atherton, C. S., Bell, N., Bergmann, D. J., Bey, I., Butler, T., Cofala, J., Collins, W. J., Derwent, R. G., Doherty, R. M., Drevet, J., Eskes, H. J., Fiore, A. M., Gauss, M., Hauglustaine, D. A., Horowitz, L. W., Isaksen, I. S. A., Krol, M. C., Lamarque, J. F., Lawrence, M. G., Montanaro, V., Müller, J. F., Pitari, G., Prather, M. J., Pyle, J. A., Rast, S., Rodriguez, J. M., Sanderson, M. G., Savage, N. H., Shindell, D. T., Strahan, S. E., Sudo, K., and Szopa, S.: Multimodel ensemble simulations of present-day and near-future tropospheric ozone, Journal of Geophysical Research-Atmospheres, 111, 10.1029/2005JD006338, 2006.

Surl, L., Palmer, P. I., and González Abad, G.: Which processes drive observed variations of HCHO columns over India?, Atmos. Chem. Phys., 18, 4549-4566, 10.5194/acp-18-4549-2018, 2018.

Szopa, S., Naik, V., Adhikary, B., Artaxo, P., Berntsen, T., Collins, W. D., Fuzzi, S., Gallardo, L., Kiendler-Scharr, A., Klimont, Z., Liao, H., Unger, N., and Zanis, P.: Short-lived Climate Forcers, in: Climate Change 2021: The Physical Science Basis. Contribution of Working Group I to the Sixth Assessment Report of the Intergovernmental Panel on Climate Change [Masson-

1618 Delmotte, V., P. Zhai, A. Pirani, S.L. Connors, C. Péan, S. Berger, N. Caud, Y. Chen, L.
1619 Goldfarb, M.I. Gomis, M. Huang, K. Leitzell, E. Lonnoy, J.B.R. Matthews, T.K. Maycock, T.
1620 Waterfield, O. Yelekçi, R. Yu, and B. Zhou (eds.)], edited by: Intergovernmental Panel on
1621 Climate, C., Cambridge University Press, Cambridge, 817-922, DOI:
1622 10.1017/9781009157896.008, 2021.

1623 Taraborrelli, D., Cabrera-Perez, D., Bacer, S., Gromov, S., Lelieveld, J., Sander, R., and
1624 and Pozzer, A.: Influence of aromatics on tropospheric gas-phase composition, Atmos. Chem.
1625 Phys., 21, 2615-2636, 10.5194/acp-21-2615-2021, 2021.

1626 Tarasick, D. W., Carey-Smith, T. K., Hocking, W. K., Moeini, O., He, H., Liu, J., Osman, M.
1627 K., Thompson, A. M., Johnson, B. J., Oltmans, S. J., and Merrill, J. T.: Quantifying
1628 stratosphere-troposphere transport of ozone using balloon-borne ozone sondes, radar wind
1629 profilers and trajectory models, Atmospheric Environment, 198, 496-509,
1630 https://doi.org/10.1016/j.atmosenv.2018.10.040, 2019.

1631 Van Vuuren, D. P., Edmonds, J., Kainuma, M., Riahi, K., Thomson, A., Hibbard, K., Hurtt, G.
1632 C., Kram, T., Krey, V., Lamarque, J.-F., Masui, T., Meinshausen, M., Nakicenovic, N., Smith,
1633 S. J., and Rose, S. K.: The representative concentration pathways: an overview, Climatic
1634 Change, 109, 5, 10.1007/s10584-011-0148-z, 2011.

1635 Veefkind, J. P., Aben, I., McMullan, K., Förster, H., de Vries, J., Otter, G., Claas, J., Eskes, H.
1636 J., de Haan, J. F., Kleipool, Q., van Weele, M., Hasekamp, O., Hoogeveen, R., Landgraf, J.,
1637 Snel, R., Tol, P., Ingmann, P., Voors, R., Kruizinga, B., Vink, R., Visser, H., and Levelt, P. F.:
1638 TROPOMI on the ESA Sentinel-5 Precursor: A GMES mission for global observations of the
1639 atmospheric composition for climate, air quality and ozone layer applications, Remote Sensing
1640 of Environment, 120, 70-83, https://doi.org/10.1016/j.rse.2011.09.027, 2012.

1641 Verstraeten, W. W., Neu, J. L., Williams, J. E., Bowman, K. W., Worden, J. R., and Boersma,
1642 K. F.: Rapid increases in tropospheric ozone production and export from China, Nature
1643 Geoscience, 8, 690-695, 10.1038/ngeo2493, 2015.

1644 Vignati, E., Wilson, J., and Stier, P.: M7: An efficient size-resolved aerosol microphysics
1645 module for large-scale aerosol transport models, Journal of Geophysical Research,
1646 Atmospheres, 109, 10.1029/2003JD004485, 2004.

1647 Wang, Y., Zhao, Y., Liu, Y. *et al.* Sustained emission reductions have restrained the ozone
1648 pollution over China. *Nat. Geosci.* **16**, 967–974 (2023). https://doi.org/10.1038/s41561-023-
1649 01284-2

1650 Wang, H., Lu, X., Jacob, D. J., Cooper, O. R., Chang, K. L., Li, K., Gao, M., Liu, Y., Sheng,
1651 B., Wu, K., Wu, T., Zhang, J., Sauvage, B., Nédélec, P., Blot, R., and Fan, S.: Global
1652 tropospheric ozone trends, attributions, and radiative impacts in 1995–2017: an integrated
1653 analysis using aircraft (IAGOS) observations, ozone sonde, and multi-decadal chemical model
1654 simulations, Atmos. Chem. Phys., 22, 13753-13782, 10.5194/acp-22-13753-2022, 2022.

1655 Wang, W., van der A, R., Ding, J., van Weele, M., and Cheng, T.: Spatial and temporal changes
1656 of the ozone sensitivity in China based on satellite and ground-based observations, Atmos.
1657 Chem. Phys., 21, 7253-7269, 10.5194/acp-21-7253-2021, 2021.

Wang, Y., Lampel, J., Xie, P., Beirle, S., Li, A., Wu, D., and Wagner, T.: Ground-based MAX-DOAS observations of tropospheric aerosols, NO2, SO2 and HCHO in Wuxi, China, from 2011 to 2014, Atmos. Chem. Phys., 17, 2189-2215, 10.5194/acp-17-2189-2017, 2017.

WMO, Meteorology – A three-dimensional science, World Meteorological Organization, Bulletin 6, (Oct), 134–138, 1957.

Young, P. J., Naik, V., Fiore, A. M., Gaudel, A., Guo, J., Lin, M. Y., Neu, J. L., Parrish, D. D., Rieder, H. E., Schnell, J. L., Tilmes, S., Wild, O., Zhang, L., Ziemke, J., Brandt, J., Delcloo, A., Doherty, R. M., Geels, C., Hegglin, M. I., Hu, L., Im, U., Kumar, R., Luhar, A., Murray, L., Plummer, D., Rodriguez, J., Saiz-Lopez, A., Schultz, M. G., Woodhouse, M. T., and Zeng, G.: Tropospheric Ozone Assessment Report: Assessment of global-scale model performance for global and regional ozone distributions, variability, and trends, Elementa: Science of the Anthropocene, 6, 10.1525/elementa.265, 2018.

Zanis, P., Akritidis, D., Turnock, S., Naik, V., Szopa, S., Georgoulias, A.K., Bauer, S.E., Deushi, M., Horowitz, L.W., Keeble, J. and Le Sager, P., 2022. Climate change penalty and benefit on surface ozone: a global perspective based on CMIP6 earth system models. Environmental Research Letters, 17(2), p.024014.

Zhang, Y. Q., Cooper, O. R., Gaudel, A., Thompson, A. M., Nédélec, P., Ogino, S. Y., and West, J. J.: Tropospheric ozone changes from 1980 to 2010 dominated by equatorward redistribution of emissions, Nature Geoscience, 9, 875-+, 10.1038/NGEO2827, 2016.

Zhang, Y., West, J. J., Emmons, L. K., Flemming, J., Jonson, J. E., Lund, M. T., et al. (2021). Contributions of World Regions to the Global Tropospheric Ozone Burden Change from 1980 to 2010. *Geophysical Research Letters*, 48, e2020GL089184. https://doi.org/10.1029/2020GL089184

Ziemke, J. R., Chandra, S., and Bhartia, P. K.: A 25-year data record of atmospheric ozone in the Pacific from Total Ozone Mapping Spectrometer (TOMS) cloud slicing: Implications for ozone trends in the stratosphere and troposphere, Journal of Geophysical Research - Atmopsheres, 110, 10.1029/2004JD005687, 2005.

Ziemke, J. R., Chandra, S., Duncan, B. N., Froidevaux, L., Bhartia, P. K., Levelt, P. F., and Waters, J. W.: Tropospheric ozone determined from aura OMI and MLS: Evaluation of measurements and comparison with the Global Modeling Initiative's Chemical Transport Model, Journal of Geophysical Reseach - Atmospheres, 111, 10.1029/2006JD007089, 2006.

Ziemke, J. R., Oman, L. D., Strode, S. A., Douglass, A. R., Olsen, M. A., McPeters, R. D., Bhartia, P. K., Froidevaux, L., Labow, G. J., Witte, J. C., Thompson, A. M., Haffner, D. P., Kramarova, N. A., Frith, S. M., Huang, L. K., Jaross, G. R., Seftor, C. J., Deland, M. T., and Taylor, S. L.: Trends in global tropospheric ozone inferred from a composite record of TOMS/OMI/MLS/OMPS satellite measurements and the MERRA-2 GMI simulation, Atmos. Chem. Phys., 19, 3257-3269, 10.5194/acp-19-3257-2019, 2019.